The surface energy balance in a cold-arid permafrost environment, Ladakh Himalaya, India

John Mohd Wani[1], Renoj J. Thayyen[2*], Chandra Shekhar Prasad Ojha[1], and Stephan Gruber[3]

[1]Department of Civil Engineering, Indian Institute of Technology (IIT) Roorkee, India, [2]Water Resources System Division, National Institute of Hydrology, Roorkee, India (renoj.nihr@gov.in; renojthayyen@gmail.com), [3]Department of Geography & Environmental Studies, Carleton University, Ottawa, Canada

Abstract

The cold-arid trans-Himalayan region comprises significant areas underlain by permafrost. While the information on the permafrost characteristics and extent started emerging, the governing energy regimes of this cryosphere region is of particular interest. This paper presents the results of Surface Energy Balance (SEB) study carried out in the upper Ganglass catchment in the Ladakh region of India, which feed directly to the River Indus. The point SEB is estimated using the one-dimensional mode of GEOtop model from 1 September 2015 to 31 August 2017 at 4727 m a.s.l elevation. The model is evaluated using field monitored snow depth variations (accumulation and melting), outgoing longwave radiation and one-year near-surface ground temperatures and showed good agreement with the respective simulated values. For the study period, the surface energy balance characteristics of the study site show that the net radiation (29.7 W m^{-2}) was the major component, followed by sensible heat flux (-15.6 W m^{-2}), latent heat flux (-11.2 W m^{-2}) and the ground heat flux was equal to -0.5 W m^{-2}. During both the years, the latent heat flux was highest in summer and lowest in winter, whereas the sensible heat flux was highest in post-winter and gradually decreased towards the pre-winter season. During the study period, snow cover builds up in the catchment initiated by the last week of December facilitating the ground cooling by almost three months (October to

December) of sub-zero temperatures up to -20 °C providing a favourable environment for permafrost. It is observed that the Ladakh region have a very low relative humidity in the range of 43% as compared to, e.g., ~70% in the Alps facilitating lower incoming longwave radiation and strongly negative net longwave radiation averaging ~ -90 W m^{-2} compared to -40 W m^{-2} in the Alps. Hence, the high elevation cold-arid region land surfaces could be overall colder than the locations with more RH such as the Alps. Further, it is apprehended that high incoming shortwave radiation in the region during summer months may be facilitating enhanced cooling of wet valley bottom surfaces as a result of stronger evaporation.

Keywords: Cold-arid, Cryosphere, GEOtop, Himalaya, Leh, Permafrost, Surface Energy Balance

1 Introduction

The Himalayan cryosphere is essential for sustaining the flows in the major rivers originating from the region (Bolch et al., 2012, 2019; Hock et al., 2019; Immerzeel et al., 2012; Kaser et al., 2010; Lutz et al., 2014; Pritchard, 2019). These rivers flow through the most populous regions of the world (Pritchard, 2019) and insight on the processes driving the change is critical for evaluating the future trajectory of water resources of the area, ranging from small headwater catchments to large river systems (Lutz et al., 2014). It is hard to propose a uniform framework for the downstream response of these rivers as they originate and flow through various glacio-hydrological regimes of the Himalaya (Kaser et al., 2010; Thayyen and Gergan, 2010). Lack of understanding of multiple processes driving the cryospheric response of the region is limiting our ability to anticipate the subsequent changes and their impacts correctly. This has been highlighted by the recent studies which suggested the occurrence of higher precipitation in the accumulation zones of the glaciers than previously known (Bhutiyani, 1999; Immerzeel et al., 2015; Thayyen, 2020).

The sensitivity of mountain permafrost to climate change (Haeberli et al., 2010) leads to changes in permafrost conditions such as an increase in active layer thickness that eventually affect the ground stability (Gruber and Haeberli, 2007; Salzmann et al., 2007), trigger debris flows and rockfalls (Gruber et al., 2004; Gruber and Haeberli, 2007; Harris et al., 2001), hydrological changes (Woo et al., 2008), run-off patterns (Gao et al., 2018; Wang et al., 2017), water quality (Roberts et al., 2017), greenhouse gas emissions (Mu et al., 2018), alpine ecosystem changes (Wang et al., 2006), and unique construction requirements to negate the effects caused by ground-ice degradation (Bommer et al., 2010). These strongly affect the mountain communities and indicate the relevance of mountain permafrost on human livelihoods. Field observations suggest that ground-ice melt may be a critical water source in dry summer years in the cold-arid regions of Ladakh (Thayyen, 2015).

The energy balance at the earth's surface drives the spatio-temporal variability of ground temperature (Oke, 2002; Sellers, 1965; Westermann et al., 2009). It is linked to the atmospheric boundary layer, and location-dependent transfer mechanisms between land and the overlying atmosphere (Endrizzi, 2007; Martin and Lejeune, 1998; McBean and Miyake, 1972). The surface energy balance (SEB) in cold regions additionally depends on the seasonal snow cover, vegetation and moisture availability in the soil (Lunardini, 1981) and (semi-) arid areas exhibit their typical characteristics (Xia, 2010).

The role of permafrost is a key unknown variable in the Himalaya, especially in headwater catchments of the Indus basin. However, one can notice that the none of excellent studies about Himalayan cryosphere (e.g., Immerzeel et al., 2010; Lutz et al., 2014) discuss permafrost and its role in regional climate and Hydrology. And this is our prime motivation to take up the permafrost studies in the region. Recent studies have signalled significant permafrost area in the cold-arid upper Indus basin areas covering Ladakh (Wani et al., 2020). This study suggests the permafrost area in a small (15.4 km^2) catchment in the Ladakh region is 22 times of the

glacier area. More coarse assessment in the Hindu Kush Himalaya (HKH) region suggests that the permafrost area extends up to 1 million km^2, which roughly translate into 14 times the area of glacier cover of the region (Gruber et al., 2017). Except for Bhutan, the expected permafrost areas in all other countries is larger than the glacier area. With two-thirds of the HKH underlain by permafrost, China has by far the largest estimated share ($906x10^3$ km^2) followed by India ($40.1x10^3$ km^2), Pakistan ($26.6x10^3$ km^2), Afghanistan ($17.5x10^3$ km^2), Nepal ($11.1x10^3$ km^2), Bhutan ($1.2x10^3$ km^2) and Myanmar ($0.1x10^3$ km^2) (cf. Table 1, Gruber et al., 2017). The mapping of rock glaciers using remote sensing suggested that the discontinuous permafrost in the HKH region can be found between 3500 m a.s.l. in Northern Afghanistan to 5500 m a.s.l. on the Tibetan Plateau (Schmid et al., 2015). Recently, Pandey (2019) published a remote sensing based rock glacier inventory of Himachal Himalaya and reports that the discontinuous permafrost can be found within an elevation range of 3000–5500 m a.s.l. Another rock glacier inventory from IHR suggests that the elevations above 4600 m a.s.l. are suitable for the occurrence of permafrost (Baral et al., 2019). Similarly, an initial localised estimate of 420 km^2 of permafrost is suggested in the Kullu district of Himachal Pradesh, India (Allen et al., 2016). The cold-arid region of Ladakh has reported sporadic occurrence of permafrost and associated landforms (Gruber et al., 2017; Wani et al., 2020) with the sorted patterned ground and other periglacial landforms such as ice-cored moraines. Previous studies of permafrost in the Ladakh region are from the Tso Kar basin (Rastogi and Narayan, 1999; Wünnemann et al., 2008), and the Changla region (Ali et al., 2018).

The SEB characteristics of different permafrost regions have been studied, e.g., the North American Arctic (Eugster et al., 2000; Lynch et al., 1999; Ohmura, 1982, 1984), European Arctic (Lloyd et al., 2001; Westermann et al., 2009), Tibetan Plateau (Gu et al., 2015; Hu et al., 2019; Yao et al., 2008, 2011, 2020), European Alps (Mittaz et al., 2000) or Siberia (Boike et al., 2008; Kodama et al., 2007; Langer et al., 2011a, 2011b). However, SEB studies of IHR

are limited, for example, the energy balance studies on glaciers by Azam et al. (2014) and Singh et al. (2020). The SEB also has a significant influence on regional and local climate (Eugster et al., 2000). During summer months, the permafrost creates a heat sink, which reduces the skin temperature, and therefore heat transfer to the atmosphere is also reduced (Eugster et al., 2000). This highlight that the knowledge of frozen ground and associated energy regimes are a critical knowledge gap in our understanding of the Himalayan cryospheric systems, especially in the Upper Indus Basin.

The goal of this manuscript is to improve the understanding of permafrost in cold-arid UIB areas and to advance our ability to analyse and simulate the characteristics of permafrost there. This can guide the application of available models in the Ladakh region which are calibrated (Boeckli et al., 2012) or validated (Cao et al., 2019; Fiddes et al., 2015) elsewhere. Furthermore, it can help to interpret differences in surface offset observed in Ladakh (Wani et al., 2020) and other permafrost areas (Boeckli et al., 2012; Hasler et al., 2015; PERMOS, 2019). Our working hypothesis is that the surface offset for particular terrain types in the UIB differs from what is known in other areas, driven by aridity and high elevation. We aim to improve the understanding of the SEB and its relationship with the ground temperature by working on three objectives: (1) Quantifying the SEB at South Pullu, as an exemplar for permafrost areas in the UIB. (2) Understand the pronounced seasonal and inter-annual variation of snowpack and GST, as these are intermediate phenomena between the SEB and permafrost. (3) Understanding key differences with other permafrost areas that have SEB observations.

2 Study area and data

2.1 Study area

The present study is carried out at South-Pullu (34.25°N, 77.62°E, 4727 m a.s.l.) in the upper Ganglass catchment (34.25°N to 34.30°N and 77.50°E to 77.65°E), Leh, Ladakh (Figure 1). Ladakh is a Union territory of India and has a unique climate, hydrology and landforms. Leh

is the district headquarter, where long-term climate data is available (Bhutiyani et al., 2007). Long-term mean precipitation of Leh (1908–2017, 3526 m a.s.l.) is 115 mm (Lone et al., 2019; Thayyen et al., 2013) and the daily minimum and maximum temperatures during the period (2010 to 2012) range between -23.4 to 33.8 °C (Thayyen and Dimri, 2014). The spatial area of the catchment is 15.4 km^2 and extends from 4700 m to 5700 m a.s.l. A small cirque glacier called as Phuche glacier with an area of 0.62 km^2 occupies the higher elevations of the catchment. A single stream flows through the valley of the catchment originating from Phuche glacier. This stream flows intermittently with most of the flow from May to October.

The catchment lies in the Ladakh mountain range and is part of the main Indus river basin. Geologically, the study catchment is part of the Ladakh batholith (Thakur, 1981). The study catchment also consists of steep mountain slopes with the valley bottom filled with glacio-fluvial deposits. Other sporadic landforms found in the catchment include patterned ground, boulder fields, peatlands, high elevation wetlands and a small lake. Many of these landforms point towards intense frost action in the area.

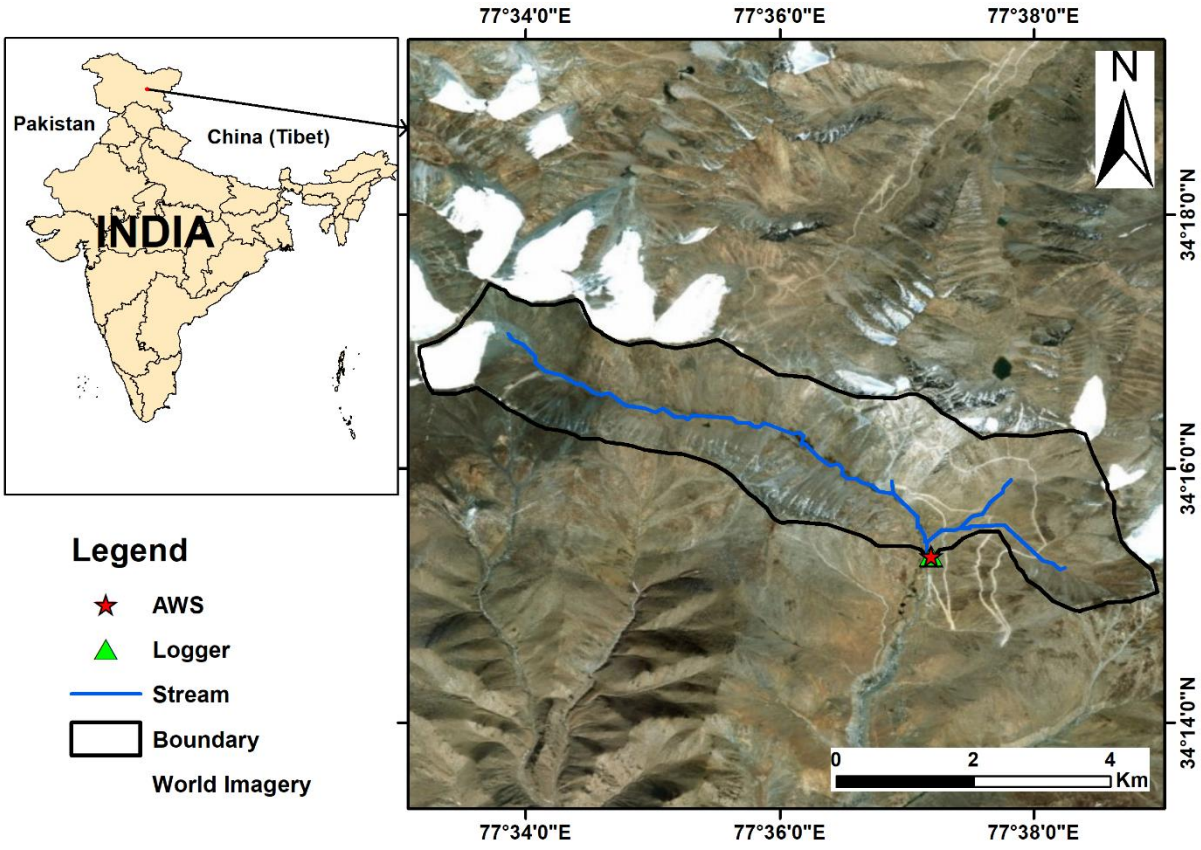

Figure 1 Location of the study site in the upper Ganglass catchment. (Base image sources on the right panel: © Esri, DigitalGlobe, GeoEye, Earthstar Geographic's, CNES/Airbus DS, USDA, USGS, AEX, Getmapping, Aerogrid, IGN, IGP, swisstopo, and the GIS User Community).

2.2 Meteorological data used

The automatic weather station (AWS) in the catchment is located at an elevation of 4727 m a.s.l. at South-Pullu (Figure 1). It is located in the wide deglaciated valley trending southeast. The site has a local slope angle of 15°, and the soil is sparsely vegetated. Weather data has been collected by a Sutron automatic weather station from 1 September 2015 to 31 August 2017. The study years 1 September 2015 to 31 August 2016 and 1 September 2016 to 31 August 2017 hereafter in the text will be designated as 2015-16 and 2016-17 respectively. The variables measured include air temperature, relative humidity, wind speed and direction, incoming and outgoing shortwave and longwave radiation and snow depth (Table 1). The snow

depth is measured using a Campbell SR50 sonic ranging sensor with a nominal accuracy of ±1 cm (Table 1). To reduce the noise of the measured snow depth, a six-hour moving average is applied. Near-surface ground temperature (GST) is measured at a depth of 0.1 m near the AWS using miniature temperature data logger (MTD) manufactured by GeoPrecision GmbH, Germany. GST data was available only from 1 September 2016 to 31 August 2017 and is used for model evaluation, only. All the four solar radiation components, i.e., incoming shortwave (SW_{in}), outgoing shortwave (SW_{out}), incoming longwave (LW_{in}) and outgoing longwave (LW_{out}) radiation were measured. Before using these data in the SEB calculations, necessary corrections were applied (Nicholson et al., 2013; Oerlemans and Klok, 2002): (a) all the values of $SW_{in} < 5\ Wm^{-2}$ are set to zero, (b) when $SW_{out} > SW_{in}$ (3 % of data understudy), it indicates that the upward-looking sensor was covered with snow (Oerlemans and Klok, 2002). The SW_{out} can be higher than SW_{in} at high elevation sites such as this one due to high solar zenith angle during the morning and evening hours (Nicholson et al., 2013). In such cases, SW_{in} was corrected by SW_{out} divided by the accumulated albedo, calculated by the ratio of measured SW_{out} and measured SW_{in} for a 24h period (van den Broeke et al., 2004).

Table 1 Technical parameters of different sensors at South-Pullu (4727 m a.s.l.) in the upper Ganglass catchment, Leh. (MF: model forcing, ME: model evaluation).

Variable	Units	Sensor	Stated accuracy	Height (m)	Use
Air temperature	(°C)	Rotronics-5600-0316-1	±0.2 °C	2.2	MF
Relative humidity	(%)	Rotronics-5600-0316-1	±1.5%	2.2	MF
Wind speed	(m s^{-1})	RM Young 05103-45	±0.3 ms^{-1}	10	MF
Wind direction	(°)	RM Young 05103-45	±0.3°	10	MF
Incoming shortwave radiation	(W m^{-2})	Kipp and Zonen (CMP6) (285 to 2800nm)	±10%	4.6	MF
Outgoing shortwave radiation	(W m^{-2})	Kipp and Zonen (CMP6) (285 to 2800nm)	±10%	4.6	MF
Incoming longwave radiation	(W m^{-2})	Kipp and Zonen (CGR3) (4500 to 42000nm)	±10%	4.3	MF
Outgoing longwave radiation	(W m^{-2})	Kipp and Zonen (CGR3) (4500 to 42000nm)	±10%	4.3	ME
Snow depth	(m)	Campbell SR-50	±1cm	3.44	ME
Data logger	-	Sutron 9210-0000-2B	-	-	-
Near-surface ground temperature	(°C)	PT1000 in stainless steel cap (by GeoPrecision GmbH, Germany)	±0.1 °C	-0.1	ME

3 Methods

3.1 Estimation of precipitation from snow height

In high elevation and remote sites, the snowfall measurement is a difficult task with an under catch of 20–50% (Rasmussen et al., 2012; Yang et al., 1999). At the South Pullu station, daily precipitation including snow was measured using a non-recording rain gauge. In this high elevation area, an under catch of 23% of snowfall was reported earlier (Thayyen et al., 2015) [Unpublished work]. Here, we had the time resolution problem between total measured precipitation and other meteorological forcing's including SR50 snow depth (hourly and recorded by automatic weather station). Therefore, to match the temporal resolution of precipitation data with other meteorological forcing's, we adopted the method proposed by Mair et al. (2016), called Estimating SOlid and Liquid Precipitation (ESOLIP). This method

makes use of snow depth and meteorological observations to estimate the sub-daily solid precipitation in terms of snow water equivalent (SWE). In ESOLIP, we considered liquid precipitation daily only. The ESOLIP method consists of following steps: (a) filtering of precipitation readings: simple criteria based on relative humidity (RH) and global shortwave radiation was used such as, for an actual precipitation event, the RH > 50% and SWin < 400 W m^{-2}, (b) precipitation type determination: wet bulb temperature (T_w) is used to differentiate between rain and snow such as if T_w < 1 (SWE estimation) and if T_w >=1 (rain). The T_w is estimated by solving the psychrometric formula implicitly: $e = E(T_w) - \gamma(T_a - T_w)$, T_a is the air temperature, and e (hPa) is the vapour pressure in the air, E (hPa) is the saturation vapour pressure, and γ (hPa K^{-1}) is the psychrometer constant depending on air pressure, (c) estimation of density: the fresh snow density (ρ) was estimated based on air temperature (T_a) and wind speed (u) as below (Jordan et al., 1999):

$$\rho = 500 * [1 - 0.951 * exp(-1.4 * (278.15 - T_a)^{-1.15} - 0.008u_{10}^{1.7})], \quad (1)$$

For 260.15 < T_a ≤ 275.65 K

$$\rho = 500 * [1 - 0.904 * \exp(-0.008u_{10}^{1.7})], \quad (2)$$

For T_a ≤ 260.15 K

and (d) estimation of SWE ($SWE = h*\rho$): to estimate the SWE of single snowfall events using snow depth measurements, and identification of the snow height increments of the single snowfall events and an accurate estimate of the snow density are necessary.

3.2 Modelling of point surface energy balance

In this study, the open-source model GEOtop version 2.0 (hereafter GEOtop) (Endrizzi et al., 2014; Rigon et al., 2006) was used for the modelling of point surface energy balance including the evolution of the snow depth and the transfer of heat and water in snow and soil. GEOtop

represents the combined ground heat and water balance, the exchange of energy with the atmosphere by taking into consideration the radiative and turbulent heat fluxes. The model has a multi-layer snowpack and solves the energy and water balance of the snow cover and soil including the highly non-linear interactions between the water and energy balance during soil freezing and thawing (Dall'Amico et al., 2011). It can be applied in complex terrain and makes it possible to account for topographical and other environmental variability (Fiddes et al., 2015; Gubler et al., 2013).

Previous studies have successfully applied GEOtop in mountain regions, e.g., simulating snow depth and ground temperature (Endrizzi et al., 2014), snow cover mapping (Dall'Amico et al., 2011b, 2018; Engel et al., 2017; Zanotti et al., 2004), ecohydrological processes (Bertoldi et al., 2010; Chiesa et al., 2014), modelling of ground temperature in complex topography (Fiddes and Gruber, 2012), water and energy fluxes (Hingerl et al., 2016; Rigon et al., 2006; Soltani et al., 2019), evapotranspiration (Mauder et al., 2018), permafrost distribution (Fiddes et al., 2015) or modelling ground temperatures (Bertoldi et al., 2010; Gubler et al., 2013).

Generally, the surface energy balance (SEB) (Eq. 3) is written as a combination of net radiation (R_n), sensible (H) and latent heat (LE) flux and heat conduction into the ground or to the snow (G) and must balance at all times (Oke, 2002):

$$R_n + H + LE + G - F_{surf} = 0 \quad (3)$$

where F_{surf} is the resulting latent heat flux in the snowpack due to melting or freezing, the sign convention adopted in this study is as, the energy fluxes towards the surface are positive, and negative if directed away from the surface (Mölg, 2004). During the summertime, when conditions for snow melting are prevailing at the ground surface, the F_{surf} is negative (loss from the system) as a result of energy available for melting snow and warming the ground under

snow free conditions. The positive F_{surf} (gain to the system) during summertime is the energy released to refreeze the water and represents the freezing flux.

In the cold regions, the SEB is a complex function of solar radiation, seasonal snow cover, vegetation, near-surface moisture content, and atmospheric temperature (Lunardini, 1981). Based on the in-situ available data, the calculation of SEB components like H, LE and G is difficult. For example, in the calculation of turbulent heat fluxes (H and LE), the wind speed and temperature measurements near the ground surface are required at two heights, which are generally not available. Therefore, parameterisation method like bulk aerodynamic method is used which is valid under statically neutral conditions in the surface layer (Stull, 1988). Hence, application of a tested model like GEOtop (Endrizzi et al., 2014; Rigon et al., 2006) is a good alternative for the estimation of these fluxes. However, in the GEOtop (Endrizzi et al., 2014), the general equation of SEB (Eq. 3) is linked with the water balance and is written as (Eq. 4):

$$F_{surf}(T_s) = SW_n + LW_n(T_s) + H(T_s) + LE(T_s, \theta_w) \quad (4)$$

where T_s, the temperature of the surface, is an unknown in the equation, SW_n is the shortwave radiation, LW_n is the net longwave radiation. The F_{surf} is a function of the T_s. Other terms in Eq. 4 which are a function of T_s include LW_n, H and LE. In addition, the LE also depends on the soil moisture at the surface (θ_w), linking the SEB and water balance equations. The equations and the key elements of GEOtop are explained in Endrizzi et al. (2014), and here, only a brief description of the equations that are of interest in this study is given. The SW_n in Eq. 4 is equal to the difference between the incoming solar radiation (SW_{in}) coming from the atmosphere and the reflected shortwave radiation (SW_{out}) (Oke, 2002). Also, LW_n in Eq. 4 is equal to the difference between the incoming longwave radiation (LW_{in}) coming from the atmosphere and the outgoing longwave radiation (LW_{out}) radiated by the surface (Oke, 2002).

The LW_{out} radiated by the surface is also estimated using the Stefan-Boltzmann law (Eq. 5), as below:

$$LW_{out} = \in_s . \sigma . T_s^4 \quad (5)$$

where T_s is the surface temperature (K) and $\in_s$ is the surface emissivity.

The turbulent fluxes (H and LE) are driven by the gradients of temperature and specific humidity between the air and the surface, and due to turbulence caused by winds as primary transfer mechanism in the boundary layer (Endrizzi, 2007). GEOtop estimates the turbulent heat fluxes H (Eq. 6) and LE (Eq. 7) using the flux-gradient relationship (Brutsaert, 1975; Garratt, 1994) as below:

$$H = \rho_a c_p w_s \frac{T_a - T_s}{r_a} \quad (6)$$

$$LE = \beta_{YP} L_e \rho_a c_p w_s \frac{Q_a - \alpha_{YP} Q_s^*}{r_a} \quad (7)$$

where ρ_a is the air density (kg m^{-3}), w_s is the wind speed (m s^{-1}), c_p the specific heat at constant pressure (J kg^{-1} K^{-1}), L_e the specific heat of vaporisation (J kg^{-1}), Q_a and Q_s^* are the specific humidity of the air (kg kg^{-1}) and saturated specific humidity at the surface (kg kg^{-1}) respectively, and r_a is the aerodynamic resistance (-). The aerodynamic resistance is obtained applying the Monin–Obukhov similarity theory (Monin and Obukhov, 1954), which requires that values of wind speed, air temperature and specific humidity are available at least at two different heights above the surface. But the values of these variables are generally measured at standard height above the surface and can be used for near surface with following assumptions: (a) the air temperature is equal to the ground surface temperature; however, this assumption leads to the boundary condition nonlinearity, (b) the specific humidity is equal to $\alpha_{YP} Q_s^*$, and (c) wind speed is equal to zero.

The β_{YP} and α_{YP} are the coefficients (Eq. 8 and 9) that take into account the soil resistance to evaporation, and only depend on the liquid water pressure close to the soil surface. They are calculated according to the parameterisation of Ye and Pielke (1993), which considers evaporation as the sum of the proper evaporation from the surface and diffusion of water vapour in soil pores at greater depths:

$$\beta_{YP} = \chi_p(g) - \frac{[\chi_p(g) - \theta_g]}{1 + \frac{\chi_p(1) - \theta_{(1)} r_a}{\chi_p(g) - \theta_g \; r_d}} \tag{8}$$

$$\alpha_{YP} = \frac{1}{\beta_{YP}} \left[\theta_g + \frac{\chi_p(1) - \theta_{(1)}}{1 + \frac{\chi_p(1) - \theta_{(1)} r_a}{\chi_p(g) - \theta_g \; r_d}} \frac{r_a}{r_d} h_{s(\theta_1)} \frac{q^{sat}_{(Ts1)}}{q^{sat}_{(Tg)}} \right] \tag{9}$$

q^{sat} is the specific humidity in the saturated condition, the subscripts g and 1 in above two equations refer to the ground surface and a thin layer next to the ground surface, respectively, θ is the volumetric water content of the soil, χ_p is the volumetric fraction of soil pores, h_s is the relative humidity in the pores, T_g is the temperature at the ground surface, r_d is the soil resistance to water vapour diffusion.

3.2.1 The heat equation and snow depth

The equation (Eq. 10) representing the energy balance in a soil volume subject to phase change in GEOtop is given below (Endrizzi et al., 2014):

$$\frac{\partial U^{\mathrm{ph}}}{\partial t} + \nabla . \mathbf{G} + S_{en} - \rho_w \left[L_f + c_{\mathrm{w}} \left(T - T_{ref} \right) \right] S_w = 0 \tag{10}$$

where U^{ph} is the volumetric internal energy of soil (J m^{-3}) subject to phase change, t(s) time, $\nabla\cdot$ the divergence operator, G the heat conduction flux (W m^{-2}), S_{en} is the energy sink term (W m^{-3}), S_w is the mass sink term (s^{-1}), L_f (J kg^{-1}) the latent heat of fusion, ρ_w the density of liquid water in soil (kg m^{-3}), c_{w} is the specific thermal capacity of water (J kg^{-1} K^{-1}), T (°C)

306 the soil temperature and T_{ref} (°C) the reference temperature at which the internal energy is
307 calculated. If G is written according to Fourier's law, the Eq. 10 becomes:

$$\frac{\partial U^{\mathrm{ph}}}{\partial t} + \nabla.(\lambda_T \nabla \mathrm{T}) + S_{en} - \rho_w\left[L_f + c_{\mathrm{w}}\left(T - T_{ref}\right)\right]S_w = 0 \qquad (11)$$

308

309 where λ_T is the thermal conductivity (W m^{-1} K^{-1}). The λ_T being a non-linear function of
310 temperature, because the proportion of liquid water and ice contents depends on temperature.
311 For the calculation of λ_T , the GEOtop uses the method proposed by Cosenza et al. (2003). The
312 detailed description of the heat conduction equation used in GEOtop can be found in Endrizzi
313 et al. (2014).
314 The snow cover buffers the energy exchange between the soil and atmosphere and critically
315 influences the soil thermal regime (Endrizzi et al., 2014). GEOtop includes a multi-layer,
316 energy-based, Eulerian snow modelling approach. In GEOtop, the equations for snow
317 modelling are similar to the ones used for the soil matrix (Endrizzi et al., 2014). The
318 discretisation of snow in GEOtop is done to describe the thermal gradients which are finer near
319 the surface (with the atmosphere) and at the bottom (with soil). In GEOtop, the effective
320 thermal conductivity at the interface of snow and ground is calculated similarly as in between
321 different soil layers using the method of Cosenza et al. (2003). In GEOtop, the fresh snow
322 density is computed using the Jordan et al. (1999) formula, which is based on air temperature
323 and wind speed. More details about the snow metamorphism compaction rates and the snow
324 discretisation in GEOtop can be found in the appendix D2 and D3, respectively of (Endrizzi
325 et al., 2014).

326 **3.2.2 Model setup and forcing's**

327 The 1D GEOtop simulation was carried out at South-Pullu (Figure 1). The soil column is 10 m
328 deep and is discretised into 19 layers, with thickness increasing from the surface to the deeper
329 layers. The top 8 layers close to the ground surface were resolved with thicknesses ranging

from 0.1 to 1 m, because of the higher temperature and water pressure gradients near the surface (Endrizzi et al., 2014), while the lowest layer is 4.0 m thick.

The snowpack is discretised in 10 layers, which are finer at the top at the interface with the atmosphere and the bottom with the soil.

The model was initialised at a uniform soil temperature of -0.5 ºC and spun up by repeatedly modelling the soil temperature down to 1 m (2 years*25 times), and then using the modelled soil temperatures as an initial condition to repeatedly simulate soil temperature down to 10 m (2 years *25 times) (c.f., Fiddes et al., 2015; Gubler et al., 2013; Pogliotti, 2011). Preliminary tests show that the minimum number of repetitions required to bring the soil column to equilibrium was 25 (Figure *S1*). The values of all the input parameters used is given in Appendix (Table A1 to A4) in the supplementary material.

The input meteorological data required for running the 1D GEOtop model include time series of precipitation, air temperature, relative humidity, wind speed, wind direction and solar radiation components and the description of the site (slope angle, elevation, aspect angle, and sky view factor) for the simulation point. The model was run at an hourly time step corresponding to the measurement time step of the meteorological data.

3.3 Model performance evaluation

While the accuracy of simulated energy fluxes cannot be quantified, the quality of GEOtop simulations is evaluated based on proxy variables such as snow depth, GST and the LW_{out}. These variables were chosen because they have not been used to drive the model, and they represent different physical processes affected by surface energy balance. For example, (a) the melt-out date of the snow depth is a good indicator showing how good the surface mass and energy balance is simulated, and (b) the GST is the result of all the processes occurring at the ground surface such as radiation, turbulence, latent and sensible heat fluxes (Gubler, 2013), and (c) LW_{out} which is governed by the temperature and emissivity at the surface and the Eq.

3 is solved in terms of skin temperature. Therefore, the LW_{out} is used as a proxy for the evaluation of SEB.

Model performance is evaluated based on the measured and the simulated time series (Gubler et al., 2012). Typically, a variety of statistical measures are used to assess the model performance because no single measure encloses all aspects of interest. In this study also, R^2 (Carslaw and Ropkins, 2012), mean bias difference (MBD) and the root mean square difference (RMSD) (Badescu et al., 2012; Gubler et al., 2012; Gueymard, 2012), MB and RMSE (Gupta et al., 1999), and NSE (Nash and Sutcliffe, 1970) were used (Eq. *S*1 to *S*6).

4 Results

4.1 Model evaluation

In this section, the capability of GEOtop to reproduce the proxy variables is evaluated. The model was evaluated based on snow depth, one-year GST and the LW_{out}. In this study, the simulation results are based on the standard model parameters obtained from the literature (Table 2 and 3, Gubler et al., 2013) and were not improved by trial and error and the same simulation results are used for model evaluation.

4.1.1 Evaluation of snowpack

Snow depth variations simulated by GEOtop are compared with observations from 1 September 2015 to 31 August 2017 (Figure 2). The model captures the peaks, start and melt-out dates of the snowpack, as well as overall fluctuations (R^2 = 0.98, RMSE = 59.5 mm, MB = 16.7 mm, NSE = 0.91, Instrument error = ±10 mm) (Figure *S*2). The maximum standing snow height (*h*) simulated by the GEOtop was 1219 mm in comparison to the 1020 mm measured in the field. In the low snow year, the maximum simulated *h* was 326 mm in comparison to the 280 mm measured in the field. During the melting period of the low and high snow years, the snow depth was slightly under-estimated. However, during the accumulation period of high snow year (2016-17), the *h* was rather overestimated by the model.

Furthermore, the performance of the ESOLIP estimated precipitation was evaluated against a controlled run with precipitation data measured in the field (Figure 2). ESOLIP is the superior approach for precipitation estimation, where snow depth and necessary meteorological measurements are available.

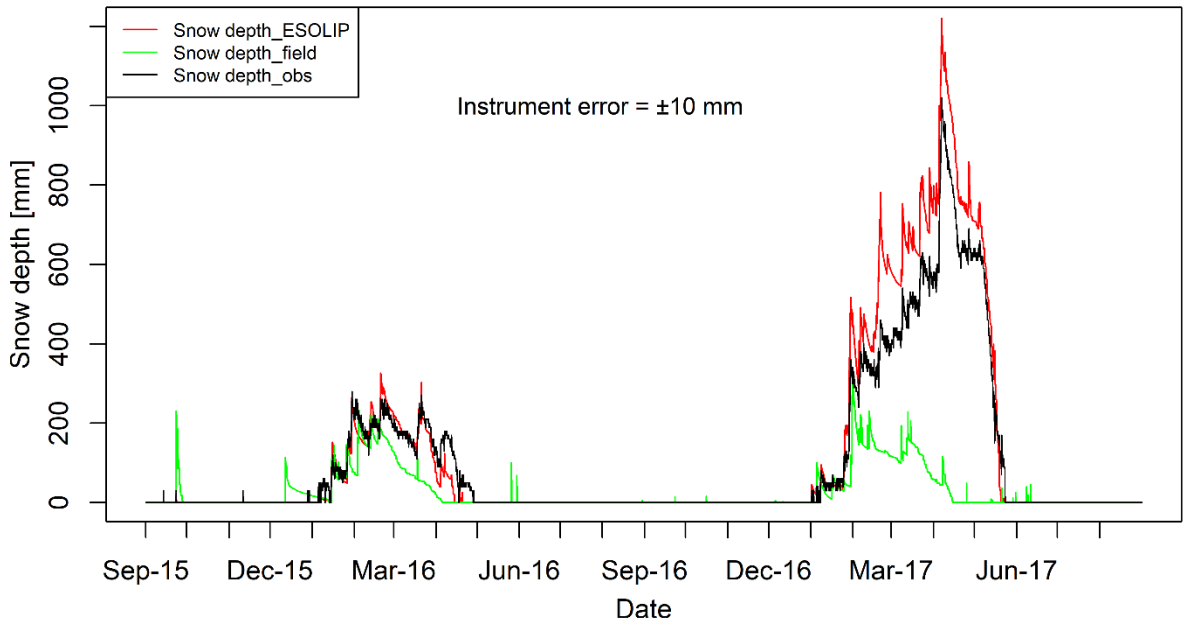

Figure 2 Comparison of hourly observed and GEOtop simulated snow depth at South-Pullu (4727 m a.s.l.) from 1 September 2015 to 31 August 2017. The black line denotes the snow depth measured in the field by SR50 sensor. The red (Snow depth_ESOLIP) and green (Snow depth_field) lines in the plot indicate the GEOtop simulated snow depth based on ESOLIP estimated precipitation and precipitation measured in the field, respectively.

4.1.2 Evaluation of near-surface ground temperatures (GST)

GST is simulated (GST_sim) on an hourly basis and compared with the observed values (GST_obs) near the AWS, available from 1 September 2016 to 31 August 2017 (Figure 3). The results show a reasonably good linear agreement between the simulated and observed GSTs (Figure *S3*, $R^2 = 0.97$, MB = -0.11 °C, RMSE = 1.63 °C, NSE = 0.95, Instrument error = ±0.1 °C). The model estimated the dampening of soil temperature fluctuations by the snowpack and the zero-curtain period at the end of melt-out of the snowpack reasonably well.

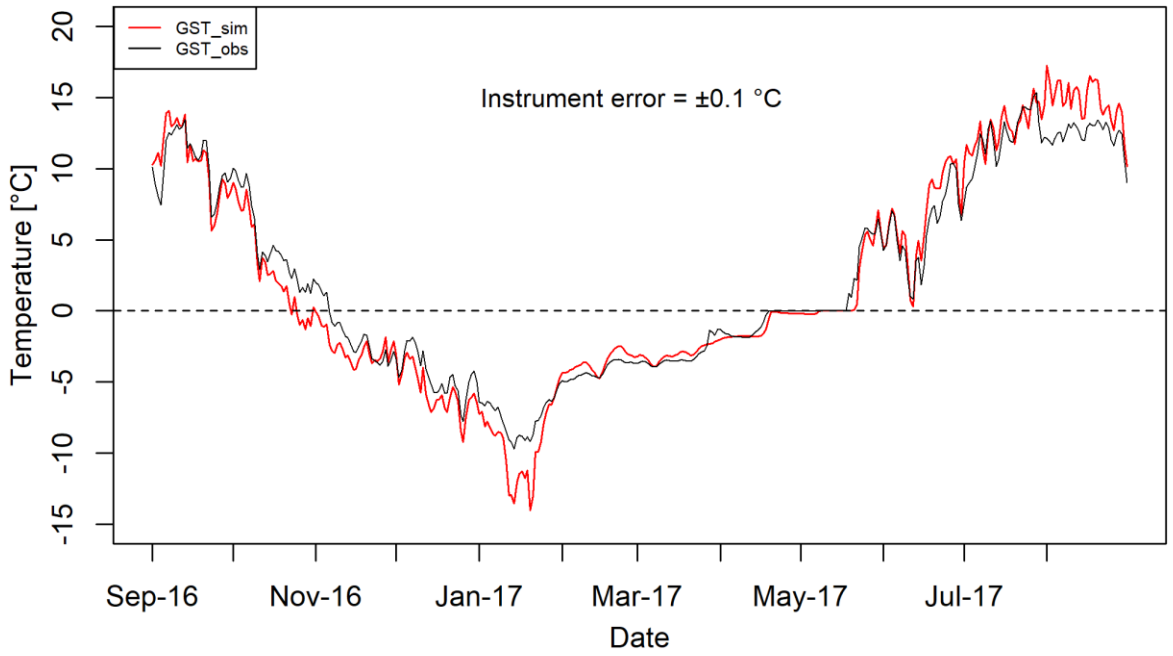

Figure 3 Comparison of daily mean observed (GST_obs, °C) and GEOtop simulated near-surface ground temperature (GST_sim, °C) at South-Pullu (4727 m a.s.l.) from 1 September 2016 to 31 August 2017.

4.1.3 Evaluation of outgoing longwave radiation

Modelled LW_{out} is evaluated with the observed measurements and a comparison of daily mean observed, and simulated LW_{out} is shown in Figure 4. The daily mean LW_{out} matches very well with the observed data, except during summer months when the simulated LW_{out} was slightly overestimated than the observed values. The hourly LW_{out} shows a good linear relationship (Figure *S*4, R^2 = 0.93, NSE = 0.73) but the GEOtop slightly overestimates the LW_{out} (MBD = 3 %) with RMSD value of 10 % (Instrument error = ±10%).

Based on the evaluation of LW_{out}, the GEOtop can simulate the surface temperature at the point scale; therefore, we believe that it can reasonably calculate the SEB components.

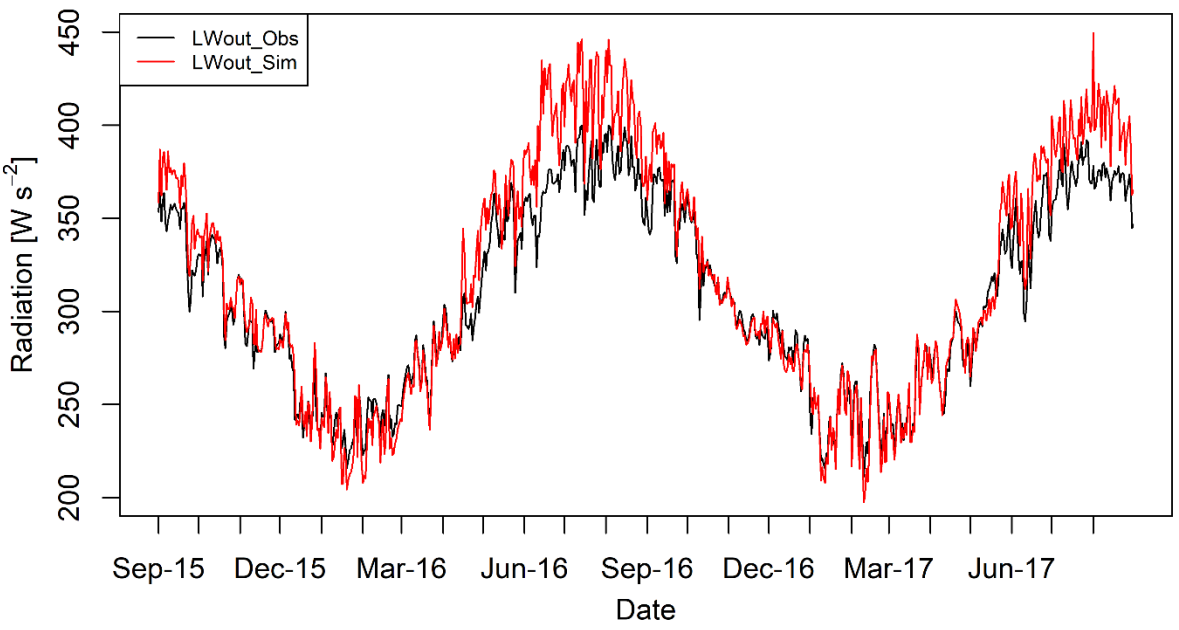

Figure 4 Comparison of daily mean observed outgoing longwave radiation (LW_{out}_obs) and GEOtop simulated (LW_{out}_sim) at South-Pullu (4727 m a.s.l.) from 1 September 2015 to 31 August 2017. The instrument error for the Kipp and Zonen (CGR3) (4500 to 42000nm) radiometer is ±10%.

4.2 Meteorological characteristics

The range of the meteorological variables measured at South-Pullu (4727 m a.s.l.) study site is given in Table 2 to provide an overview of the prevailing weather in the study region. The daily mean air temperature (T_a) throughout the study period varies between -19.5 to 13.1 °C with a mean annual average temperature (MAAT) of -2.5 °C (Figure 5A). The T_a shows significant seasonal variations and instantaneous hourly temperature at the study site range between -23.7 °C in January and 18.1 °C in July. During the two-year study period, sub-zero mean monthly temperature prevailed for seven months from October to April in both the years (2015-16 and 2016-17). The monthly mean T_a during pre-winter months (September to December) of 2015-16 and 2016-17 was −4.6 and -2.7 °C respectively. During the core winter months (January to February) of 2015-16 and 2016-17, the respective monthly mean T_a was -13.1 and -13.7 °C, for post-winter months (March and April), mean monthly T_a was -5.8 and -8 °C, respectively.

For summer months (May to August), the respective monthly mean T_a was 6.6 and 5.5 °C. A sudden change in the mean monthly T_a characterises the onset of a new season, and the most evident inter-season change was found between the winter and summer with a difference of about 16 °C during both the years.

The mean daily GST recorded by the logger near the AWS available for one year (1 September 2016 to 31 August 2017) is also plotted along with air temperature (Figure 5A). The mean daily GST ranges from -9.7 to 15.4 °C with mean annual GST of 2.1 °C. The instantaneous hourly GST at the study site range between -10.7 °C in December and 20.2 °C in July. The GST followed the pattern of air temperature, but during winter, the snow cover dampened the pattern. The GST was higher than the T_a except for a short period during snowmelt. The snow depth shown in Figure 5A is described in sub-section 4.3.

Mean relative humidity (RH) was equal to 43% during the study period (Figure 5B). The daily average wind speed (u) ranges between 0.6 (29 January 2017) to 7.1 m s^{-1} (6 April 2017) with a mean wind speed of 3.1 m s^{-1} (Figure 5C). The instantaneous hourly u was plotted as a function of wind direction (WD) (Figure *S5*) for the study period which shows that there is a persistent dominance of katabatic and anabatic winds at the study site, which is typical of a mountain environment. The average WD during the study period was southeast (148°) (Figure 5D).

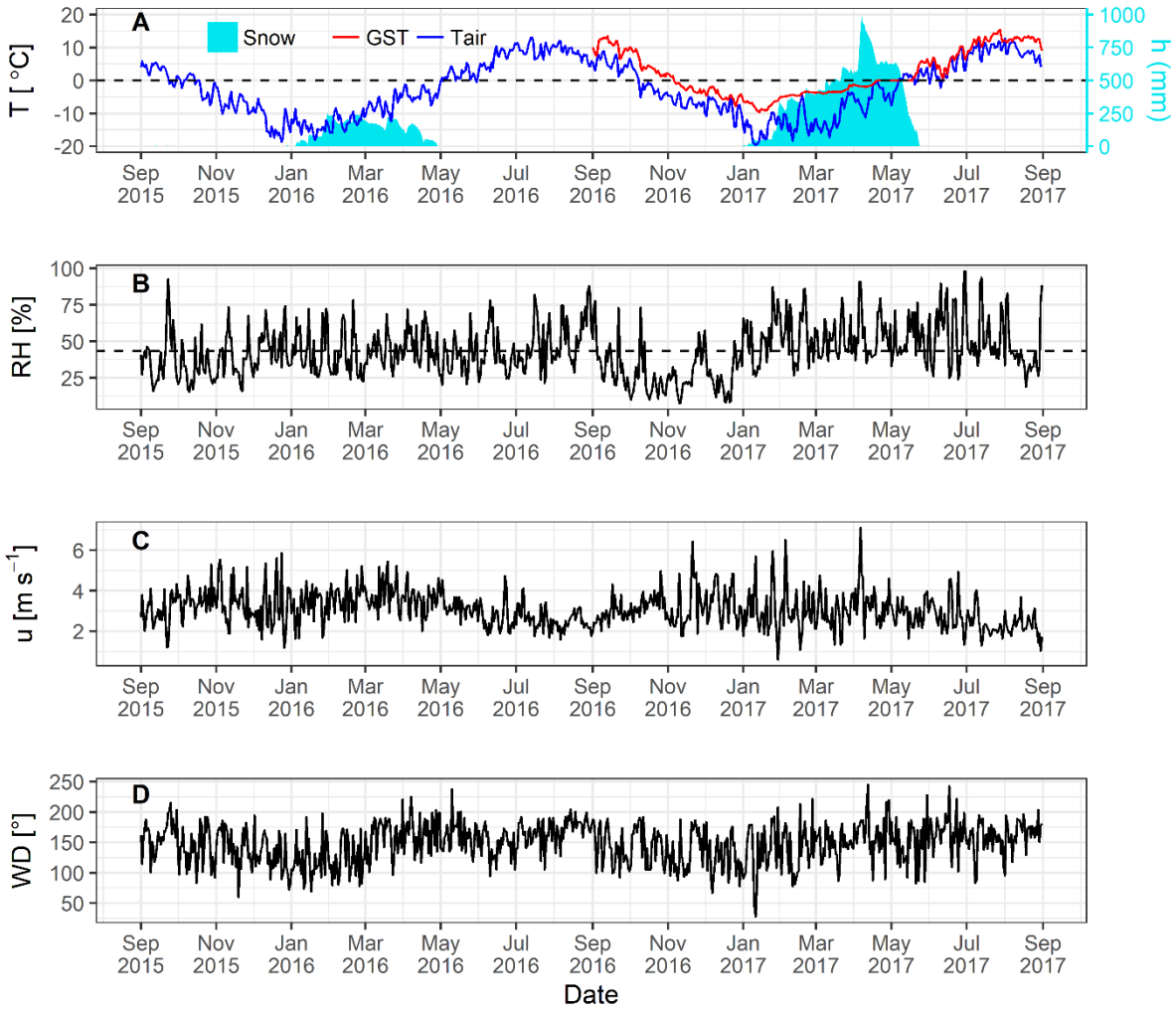

445

446 Figure 5 Daily mean values of observed (A) air temperature (blue) and one-year GST (red) (T,
447 °C), snow depth (mm) on the secondary axis; (B) relative humidity (RH, %) with a dashed line
448 as mean RH; (C) wind speed (u, ms^{-1}); and (D) wind direction (WD, °); at South-Pullu (4727
449 m a.s.l.) in the upper Ganglass catchment, Leh from 1 September 2015 to 31 August 2017.

450 The daily measured total precipitation at the study site equals 97.8 and 153.4 mm w.e. during
451 the years 2015–16 and 2016–17 respectively. After adding 23% under catch (Thayyen et al.,
452 2015) [unpublished work] to the total snow measurements, the total precipitation amount equal
453 to 120.3 and 190.6 mm w.e. for the years 2015–16 and 2016–17 respectively. During the study
454 period, the observed highest single-day precipitation was 20 mm w.e. recorded on 23
455 September 2015 and the total number of precipitation days were limited to 63. The snowfall

occurs mostly during the winter period (December to March) with some years witnessing extended intermittent snowfall till mid-June, as experienced in this study during the year 2016-17.

The precipitation estimated by the ESOLIP approach at the study site equals 92.2 and 292.5 mm w.e. during the years 2015–16 and 2016–17 respectively. The comparison between observed precipitation (mm w.e.) and the one estimated by the ESOLIP approach is given in (Table *S1*). In Table *S1*, the difference between the observed precipitation (mm w.e.) and the one estimated by the ESOLIP approach is mainly due to the under-catch of winter snow recorded by the Ordinary Rain Gauge.

4.3 Observed radiation components and snow depth

The observed daily mean variability of different components of radiation, albedo and snow depth from 1 September 2015 to 31 August 2017 at South-Pullu (4727 m a.s.l.) is shown in Figure 6. Daily mean SW_{in} varies between 24 and 378 W m^{-2} (Table 2). Highest hourly instantaneous short wave radiation recorded during the study period was 1358 W m^{-2}. Such high values of SW_{in} are typical of a high elevation arid-catchment (e.g., MacDonell et al., 2013). Persistent snow cover during the peak winter period for both the years extending from January to March resulted in a strong reflection of SW_{in} radiation (Figure 6A). During most of the non-snow period, mean daily SW_{out} radiation (Figure 6A) remain more or less stable below 100 W m^{-2}. Daily mean SW_{out} varies between 2.4 and 262.6 W m^{-2} with a mean value of 83.3 W m^{-2} (Table 2). The daily mean LW_{in} shows high variations and ranges between 109 and 345 W m^{-2} with an average of 220 W m^{-2} (Figure 3B, Table 2). Whereas LW_{out} was relatively stable and varied between 211 and 400 W m^{-2} with an average of 308 W m^{-2} (Figure 6B, Table 2). The LW_{out} shows higher daily fluctuations during the summer months as compared to the core winter months. The daily mean SW_n during the study period ranges between 2.5 and 319 W m^{-2} with a mean value of 127 W m^{-2}. The SW_n follows the pattern of $SW_{in,}$ and for both the years,

481 during the wintertime, the SW_n was close to zero due to the high reflectivity of snow (Figure
482 3C). The daily mean LW_n varies between -163 and 17 W m^{-2}. The LW_n does not show any
483 seasonality and remain more or less constant with a mean value of -88 W m^{-2} (Figure 6C). The
484 mean daily observed R_n ranges from -80.5 to 227.1 W m^{-2} with a mean of 39.4 W m^{-2} (Table
485 2). During both the years 2015–16 and 2016–17, the R_n was high in summer and autumn but
486 low in winter and spring. From January to early April (2015–16) and January to early May
487 (2016–17), when the surface was covered with seasonal snow, the R_n rapidly declined to low
488 values, or even became negative (Figure 6D). Albedo (α) is calculated as the ratio of daily
489 mean SW_{out} to daily mean SW_{in}. The α is of particular importance in the SEB and in the Earth's
490 radiation balance that dictates the rate of heating of the land surface under different
491 environmental conditions (Strugnell and Lucht, 2001). The daily mean observed α at the study
492 site ranges from 0.04 to 0.95, with a daily mean value of 0.43 (Table 2). However, the value of
493 broadband albedo is not greater than 0.85 (Roesch et al., 2002), and the maximum value (0.95)
494 recorded at the study site might be due to the instrumental error. The daily mean α was low in
495 summer and high in winter and increased significantly when the ground surface was covered
496 with snow (Figure 6E).
497 Both the years (2015–16 and 2016–17) experienced contrasting snow cover characteristics
498 during the study period (Figure 6F). The year 2015-16 experienced low snow as compared to
499 2016-17. During the 2015-16 year, the snowpack had a maximum depth of 258 mm on 30
500 January 2016, whereas, during the 2016-17 year, the maximum was 991 mm on 07 April 2017.
501 The snow cover duration was 120 days during low snow year (2015-16) and 142 days during
502 the high snow year (2016–17). The site became snow-free on 27 April in 2016 and on 23 May
503 in 2017. Higher elevations of the catchment become snow-free around 15 July in 2016 while
504 the snow cover at glacier elevations persisted till 22 August in 2017. For both the year's snow

505 cover at lower elevations initiated by the end of December and the catchment experienced sub-
506 zero mean monthly temperatures since October.

507 Table 2 Two year range of observed daily mean radiation components (SW_{in}, SW_{out}, LW_{in} and
508 LW_{out}, SW_n, LW_n), surface albedo (α), net shortwave and longwave radiation (SW_n and LW_n),
509 air temperature (T_a), wind speed (*u*), relative humidity (RH), precipitation (P), and snow depth
510 (h) for the study period (1 September 2015 to 31 August 2017) at South-Pullu (4727 m a.s.l.).

Variable	**Units**	**Min.**	**Max.**	**Mean**
SW_{in}	W m^{-2}	24.1	377.8	210.4
SW_{out}	W m^{-2}	(-)2.4	(-)262.6	(-)83.4
α	-	0.04	0.95	0.43
LW_{in}	W m^{-2}	109.0	344.7	220.4
LW_{out}	W m^{-2}	(-)211.3	(-)400.0	(-)308.0
SW_n	W m^{-2}	2.5	318.7	127.0
LW_n	W m^{-2}	-163	17.1	-87.6
T_a	°C	-19.5	13.1	-2.5
u	m s^{-1}	0.6	7.1	3.1
RH	%	8	98	43.3
P	mm w.e	0	24.6	3
h	mm	0	991	-

511

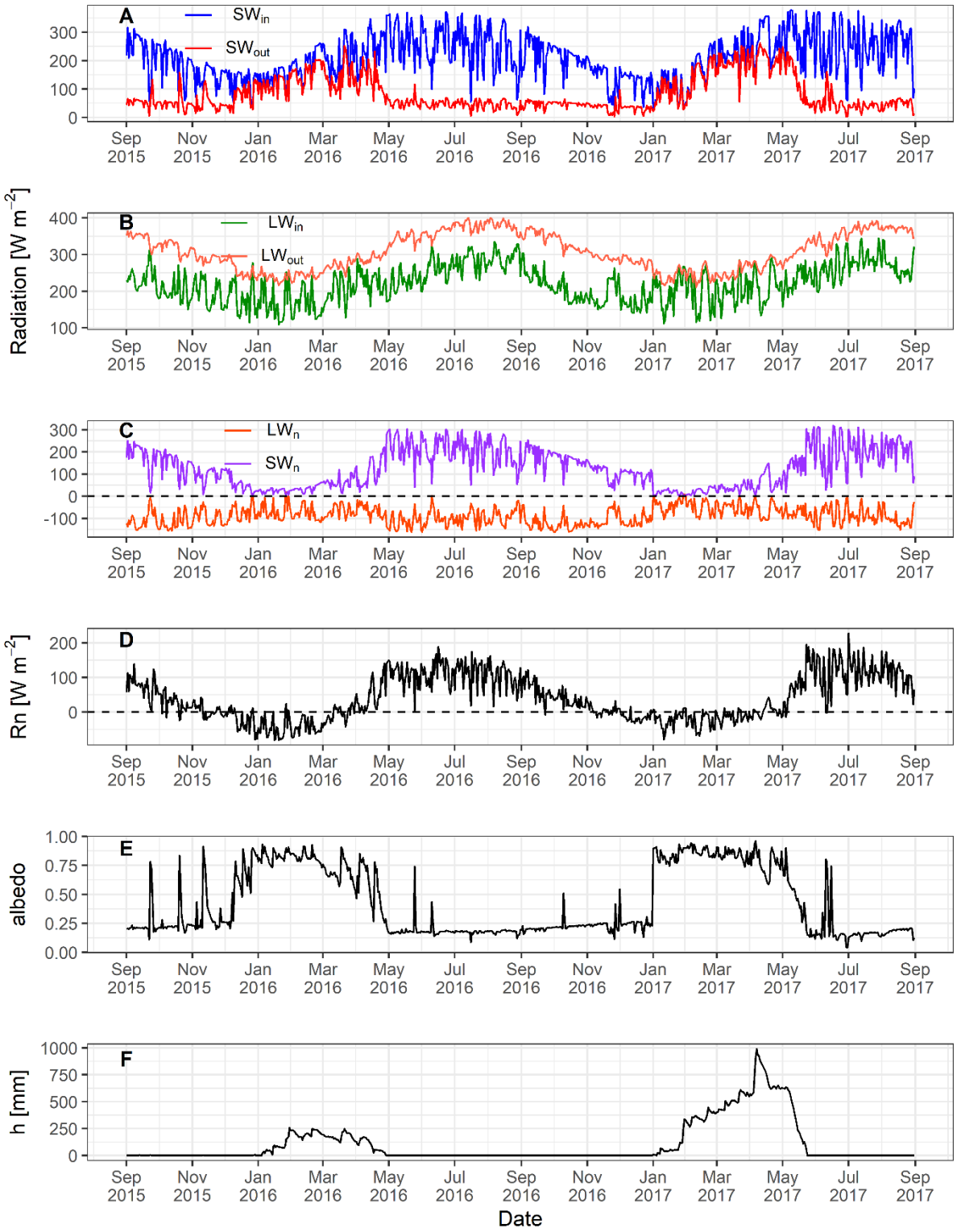

Figure 6 Observed daily mean values of (A) incoming (SW_{in}) and outgoing (SW_{out}) shortwave radiation, (B) incoming (LW_{in}) and outgoing longwave (LW_{out}) radiation, (C) net shortwave (SW_n) and longwave radiation (LW_n), and (D) net radiation (R_n), (E) surface albedo and (F) snow depth (h, mm) at South-Pullu (4727 m a.s.l.) from 1 September 2015 to 31 August 2017.

4.4 Modelled surface energy balance

The mean daily variability of modelled surface energy balance (SEB) components is shown in Figure 7. The average daily simulated R_n ranges between -78.9 to 175.6 W m^{-2} with a mean value of 29.7 W m^{-2}. The R_n shows the seasonal variability and decreases as the ground surface gets covered by seasonal snow cover during wintertime, and increases as the ground surface become snow-free (Figure 7A). From December to March of both the years (2015-16 and 2016-17), R_n decreases and is negative during snow accumulation and remains close to zero during the melting time. For the rest of the time, R_n remains positive. The simulated R_n matches the observed R_n (Figure 7A), which shows that the LW_{out} was estimated very well by the model. The daily mean H ranges between -88.6 to 53 W m^{-2} with a mean value of -15.6 W m^{-2}. The H is positive from January to April (2015-16) and January to June (2016-17) due to the presence of seasonal snow cover (Figure 7B). Rest of the period H remain negative and larger (~35 W m^{-2}) for most of the time. The seasonal variation in H points to a broader temperature gradient in summer than in winter. The daily mean LE ranges between -81.4 to 7.6 W m^{-2} with a mean value of -11.2 W m^{-2}. During the snow-free freezing period (October to December) of both the years, the LE increases (from negative to zero) due to the freezing of moisture content in the soil and also fluctuates close to zero. Furthermore, when the seasonal snow is on the ground, the LE is negative, indicating sublimation and keeps increasing (more negative) after snowmelt indicating evaporation is taking place.

The heat conduction into the ground G remains relatively a smaller component in the SEB (Figure 7C). The mean daily G ranges between -70.9 to 46.3 W m^{-2} with a mean value of -0.5 W m^{-2}. The sign of the G, which shifted from negative during summer to positive during winter, is a function of the annual energy cycle. The heat flux available at the surface for melting (F_{surf}) ranges between -137 to 46.3 W m^{-2} with a mean value of -2.8 W m^{-2} (Table 3). During the summer, when snow melting conditions were prevailing, the F_{surf} turns negative as a result of

energy available for melt (Figure 7C). The positive F_{surf} during summertime (when melting conditions are prevailing at the surface) is the energy used to refreeze the meltwater and represents the freezing heat flux.

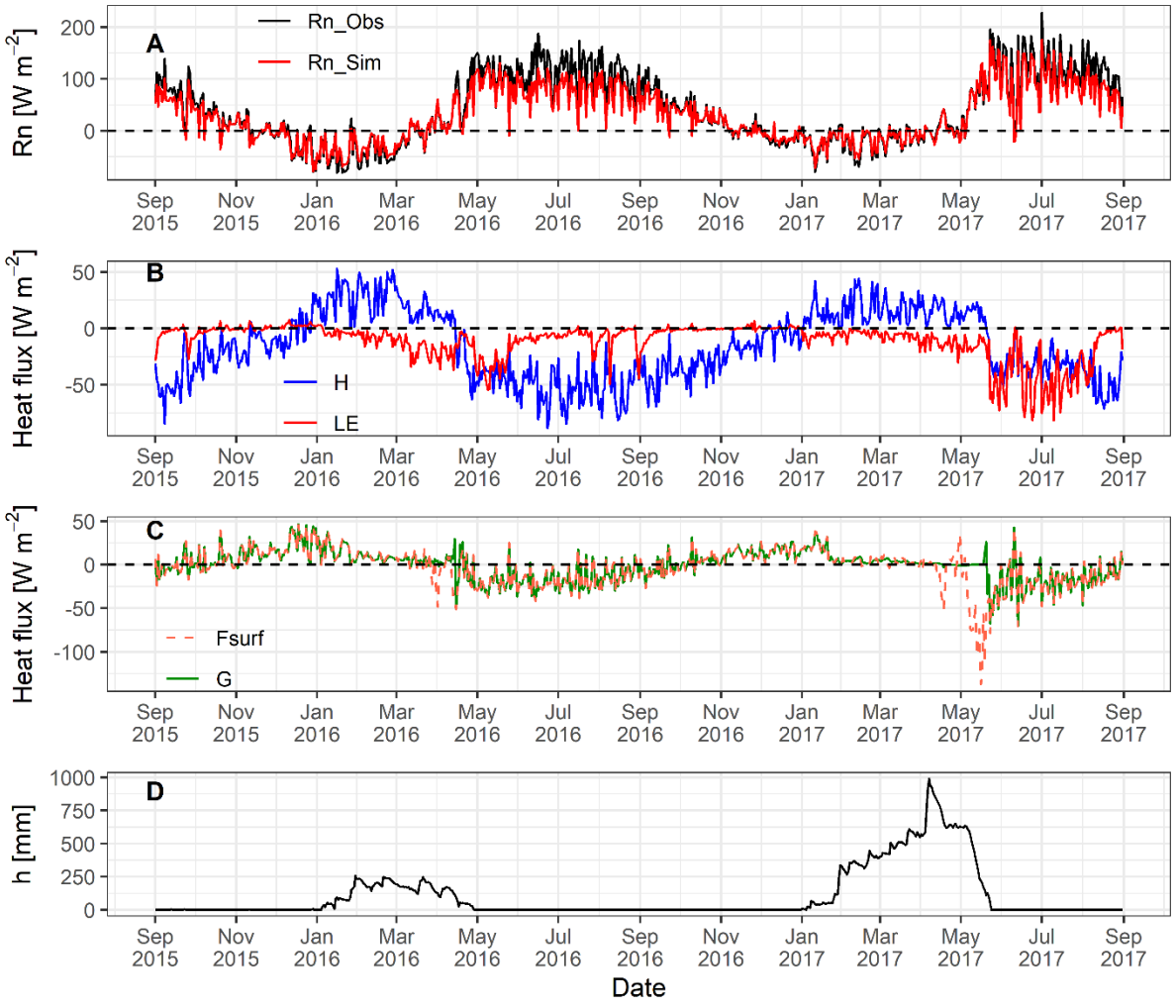

Figure 7 GEOtop simulated daily mean values of surface energy balance components (A) observed and simulated net radiation (R_n), (B) sensible (H) and latent (LE) heat flux, (C) ground heat flux (G) and surface heat flux (F_{surf}) and (D) snow depth (h) at South-Pullu (4727 m a.s.l.) from 1 September 2015 to 31 August 2017.

553 Table 3 Mean daily range of GEOtop simulated SEB (W m^{-2}) components for the study period
554 (1 September 2015 to 31 August 2017) at South-Pullu (4727 m a.s.l.).

Variable	Min.	Max.	Mean
R_n	-78.9	175.6	29.7
H	-88.6	53.0	-15.6
LE	-81.4	7.6	-11.2
G	-70.9	46.3	-0.5
F_{surf}	-137.0	46.3	-2.8

555

556 The average season diurnal variation of modelled SEB components (R_n, LE, H and G) for the
557 2015–16 and 2016–17 years are shown in Supplementary Figures *S6* and *S7*, respectively. The
558 seasons chosen were pre-winter (Sep to Dec), winter (Jan to Apr), post-winter (May-Jun), and
559 summer (Jul to Aug).

560 In the 2015–16 year (Figure *S6*), the amplitude of R_n and the G during pre-winter, post-winter
561 and summer season were the largest and smallest in winter. The G peaks earlier than those of
562 the LE and H during the pre-winter, post-winter and summer season. The LE and H show strong
563 seasonal characteristics such as (a) during the pre-winter season, the magnitude of diurnal
564 variation of H was greater than LE depicting lesser soil moisture content because of freezing
565 conditions at that time, (b) during the winter season, the amplitude of LE was slightly greater
566 (sublimation process) than H, (c) during the post-winter, the amplitude of H was greater than
567 LE and, (d) during the summer season, again the amplitude of H was greater than LE, which is
568 similar to that of the pattern seen during the pre-winter season. In the 2015-16 year, the
569 amplitude of LE in comparison to H was smaller in summer season due to the lesser
570 precipitation and lesser moisture availability. The R_n and G increased rapidly after the sunrise
571 and changed the direction during pre-winter, post-winter and summer seasons. After sunset,
572 the R_n and G again change sign rapidly, but the LE and H gradually decreased to lower values.

The LE and H in the morning increased 1 to 2 hours after the R_n during pre-, post-winter and summer season.

In the 2016–17 year (Figure *S7*), the pre-winter, winter and summer were the same as that of the 2015–16 year except for the amplitude of LE in was larger in summer season due to the more precipitation and more moisture availability. However, during the winter and post-winter season of the 2016–17 year, the main difference in diurnal changes was found because of the extended snow cover till May during that year. The amplitude of R_n, LE, H and G were smaller compared to the 2015-16 year.

During the study period, the proportional contribution shows that the net radiation component dominates (80%) the SEB followed by H (9%) and LE fluxes (5%). The G was limited to 5% of the total flux, and 1% was used for melting the seasonal snow. The proportional contribution of each flux percentages of the energy fluxes was calculated by following the approach of Zhang et al. (2013). The mean monthly modelled SEB components for both the years are given in Table *S2*.

Furthermore, during the study period, the partitioning of energy balance shows that 52% (-15.6 W m^{-2}) of R_n (29.7 W m^{-2}) was converted into H, 38% (-11.2 W m^{-2}) into LE, 1% (-0.5 W m^{-2}) into G and 9% (-2.8 W m^{-2}) for melting of seasonal snow. The partitioning was calculated by taking the mean annual average of each of the individual SEB components (LE, H and G) and then divide these respective averages with the mean annual average of R_n. However, a distinct variation of energy flux is observed during the month of May-June, when one of the years (2016-17) experienced extended snow.

4.5 Comparison of seasonal distinction of SEB during low and high snow years

A seasonal distinction of observed radiation (SW_{in}, LW_{in}, SW_{out}, LW_{out}, SW_n, LW_n,) and modelled SEB components (R_n, LE, H, G and F_{surf}) for the low and high snow years of the

study period is analysed (Table 4). The seasons were defined as winter (Sep-April) and summer (May-Aug) (Table 4). These seasons were further divided into two sub-seasons each such as early winter (Sep, Oct, Nov and Dec) and peak winter with snow (Jan, Feb, Mar and Apr). Similarly, the summer season was divided into two sub-seasons called early summer (May and June; some years with extended snow) and peak summer (July and August).

Table 4: Mean seasonal values of observed radiation and modelled surface energy balance components.

SEB Components [$W\ m^{-2}$]	2015-16				2016-17			
	Winter (Sep to Apr)		Summer (May to Aug)		Winter (Sep to Apr)		Summer (May to Aug)	
	Sep to Dec (Non-Snow)	Jan to Apr (Snow)	May to Jun (Non-Snow)	Jul-Aug (Peak Summer)	Sep to Dec (Non-Snow)	Jan to Apr (Snow)	May to Jun (Extended Snow)	Jul-Aug (Peak Summer)
SW_{in}	177.7	196.0	271.3	245.8	179.2	192.1	262.9	253.7
LW_{in}	203.0	190.5	244.5	286.5	198.0	202.5	245.9	277.0
SW_{out}	57.5	135.4	49.9	44.3	41.0	156.4	86.7	43.7
LW_{out}	310.3	259.5	379.1	412.4	317.9	251.9	337.9	399.3
SW_n	120.2	60.5	221.4	201.5	138.3	35.7	176.2	210.0
LW_n	-107.2	-69.0	-134.5	-125.9	-119.9	-49.4	-92.0	-122.3
R_n	12.9	-8.5	86.9	75.6	18.4	-13.7	84.2	87.7
LE	-1.2	-11.5	-18.9	-7.5	-1.1	-7.7	-33.1	-31.5
H	-21.7	15.7	-47.6	-54.0	-24.3	16.1	-15.9	-40.0
G	10.0	6.8	-20.3	-14.1	7.0	6.2	-14.6	-16.3
F_{surf}	0.1	2.5	0.0	0.1	0.0	0.9	20.6	0.0

The mean seasonal variability of energy fluxes during these four major seasons is shown in Table 4. The mean seasonal SW_{in} were comparable for all the seaons whereas SW_{out} was significantly higher (86.7 W m^{-2}) during early summer season of 2016-17 period on account of extended snow cover as compared to the preceeding low snow year (49.9 W m^{-2}). Similarly, LW_{in} show comparable seasonal values during the observation period and LW_{out} show a major difference during the early summer season with extended snow in 2016-17 reducing LW_{out} (337.9 W m^{-2}) as compared to corresponding period in 2015-16 (379.1 W m^{-2}).

Both the years observed comparable SW_n during the early winter period. However, during the peak snow season of the 2016-17 year, the SW_n was comparatively smaller (35.7 W m^{-2}) as

614 compared to 2015-16 (60.5 W m^{-2}) . Similarly, comparable SW_n during the peak summer
615 season of both the years is contrasted by lower SW_n (176.2 W m^{-2}) of early summer period of
616 2017 as compared to 221.4 W m^{-2} in 2016 on account of extended snow cover. The same trend
617 is recorded for LW_n as well with a lower value during the extended snow (-92 W m^{-2}) in 2017
618 as compared to 2016 (-134.5 W m^{-2}). Seasonal variations in R_n followed the pattern of SW_n.
619 Both the year's observed comparable R_n during the early snow-free winter period. However,
620 the R_n was comparatively lower (-13.7 W m^{-2}) during the peak snow season of 2016-17 as
621 compared to 2015-16 (-8.5 W m^{-2}). However, most significant difference of R_n is observed
622 during early summer (May-June) and peak summer (Jul-Aug) of 2016 and 2017, respectively.
623 Both the years observed comparable LE flux during the winter season. A key difference in LE
624 flux is observed during extended snow and peak summer sub-season of 2016 and 2017. In the
625 peak summer sub-season of 2016-17, the LE was higher (-31.5 W m^{-2}) as compared to the
626 2015-16 (-7.5 W m^{-2}). The reason behind this is due to the lesser amount of soil water content
627 availability for evaporation during 2015-16 in comparison to high snow year 2016-17. The
628 comparatively larger LE during the snow sub-season of both the years shows that sublimation
629 is a key factor in the region. The H flux was comparable during the winter season of both the
630 years. During the peak summer sub-season of the 2015-16 year, the H was slightly larger (-54
631 W m^{-2}) as compared to 2016-17 (-40 W m^{-2}). The critical difference in H flux was observed
632 during the extended snow sub-season of the 2016-17 year when H was much smaller (-15.9 W
633 m^{-2}) compared to 2015-16 (-47.6 W m^{-2}) owing to the extended snow cover during the 2016-
634 17 year.
635 During the winter season of both the years, the G was positive and changed the sign to negative
636 during the summer season. Overall, G is comparatively a smaller component. The mean
637 seasonal F_{surf} was almost equal to zero during all the seasons except during the snow sub-season
638 of both the years and extended snow sub-season of the 2016-17 year. The F_{surf} (heat flux

639 available for melt) was much higher (20.6 W m^{-2}) during the extended snow sub-season of the
640 2016-17 year. From the inter-year seasonal comparison, it was found that the extended snow
641 sub-season of the 2016-17 (high snow year) forced significant differences in energy fluxes
642 between the years.

643 # 5 Discussion

644 ## 5.1 A distinction of SEB variations during low and high snow years

645 Realistic reproduction of seasonal and inter-annual variations in snow depth during the low
646 (2015–16) and high snow (2016–17) years points towards the credible simulation of the SEB
647 during the study period. We further investigated the response of SEB components during these
648 years with contrasting snow cover for a better understanding of the critical periods of
649 meteorological forcing and its characteristics.

650 To understand the critical periods of meteorological forcing and its effect on modelled SEB
651 fluxes, we will discuss the diurnal variation of modelled SEB only for one season, i.e., early
652 summer season, which showed significant differences in the amplitude of energy fluxes
653 (Figure 8). During the early winter, peak winter and peak summer seasons (Figure *S6*, *S7*), the
654 diurnal variations of the SEB fluxes for the 2015-16 year were more or less similar in
655 comparison to the 2016-17 year. However, during the early summer season of both the years
656 (Figure 8), the SEB fluxes show different diurnal characteristics. During early summer season
657 of the 2016–17 year, the main difference in diurnal changes was found because of the extended
658 snow cover till May during that year. For the 2016–17 year, the amplitude of R_n was slightly
659 larger, whereas, all other components (LE, H and G) were of almost zero amplitude (Figure
660 8B). The smaller amplitude of LE, H and G is due to the smaller input (solar radiation) and the
661 extended seasonal snow on the ground. Therefore, we can say that the different SEB
662 characteristics during these two years' is in response to the forcing of precipitation via snowfall.

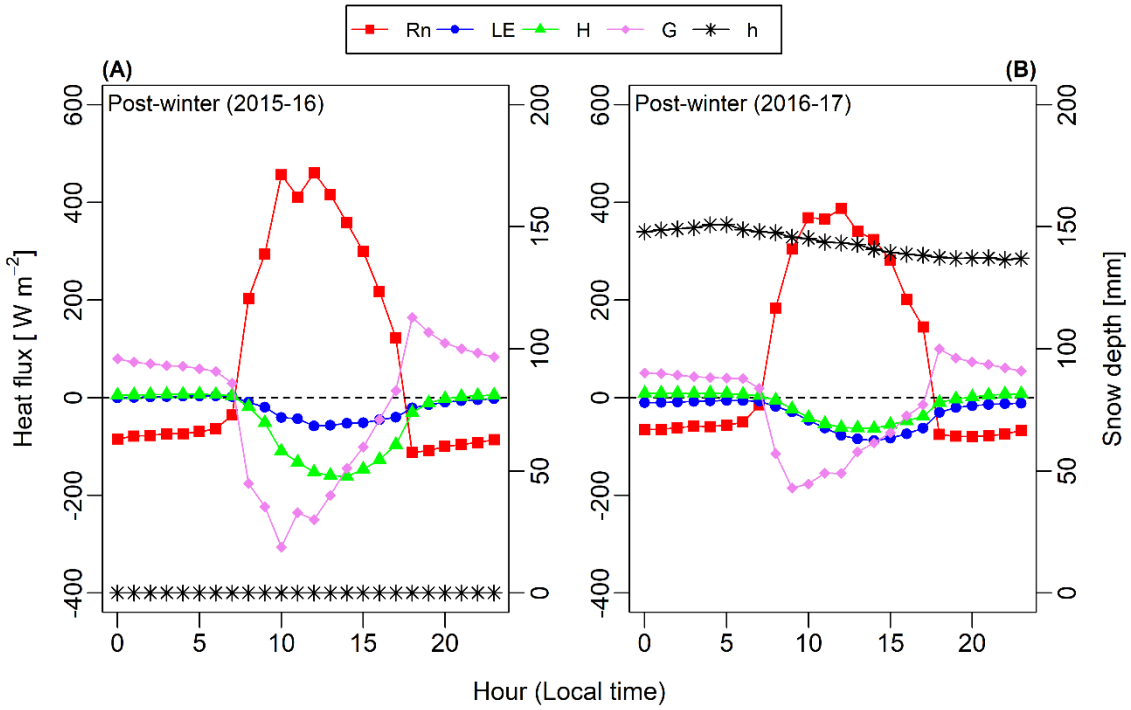

663

664 Figure 8 The diurnal change of GEOtop modelled seasonal surface energy fluxes for (A) early
665 summer 2015-16, and (B) early summer 2016-17 at South-Pullu (4727 m a.s.l.), in the upper
666 Ganglass catchment, Leh. The seasonal snow depth is plotted on the secondary axis.

667 **5.2 Impact of freezing and thawing process on surface energy fluxes**

668 To understand the impact of freeze/thaw processes on surface energy fluxes, the variability of
669 SEB components is discussed here (Figure 9). The aim is to make the study site as an exemplar
670 of SEB processes for the seasonal frozen ground and permafrost in the cold-arid Indian
671 Himalayan Region. Comparatively, the R_n was higher at the study site due to the higher
672 elevation, aridity and sparse vegetation.

673 The freeze and thaw processes in the ground are complex and involve several physical and
674 chemical changes which include energy exchange, phase change, etc. (Chen et al., 2014; Hu et
675 al., 2019). These processes amplify the interaction of fluxes between soil and atmosphere
676 (Chen et al., 2014). In Figure 9D, during the seasonal freezing phase from September to
677 December, the simulated mean monthly G starts to decrease and begins to change the sign from

678 negative to positive due to the transfer of flux from soil to the atmosphere. However, during
679 summers, the permafrost and the seasonally frozen soil act as a heat sink, because the thawing
680 processes require a considerable amount of heat that is absorbed from the atmosphere to the
681 soil (Eugster et al., 2000; Gu et al., 2015). In Figure 9D, during the thawing phase from April
682 to July, the simulated mean monthly G starts to increase and changes sign due to the transfer
683 of flux from the atmosphere to the soil. This pattern is consistent with the studies on permafrost
684 areas from the Tibetan Plateau (Chen et al., 2014; Hu et al., 2019; Zhao et al., 2000). In both
685 low and high snow years (Figure 9B and 9C), the mean monthly estimated H and LE heat
686 fluxes show prominent seasonal characteristics, such as the latent heat flux was highest in
687 summer and lowest in winter. In contrast, the sensible heat flux was highest in early summer
688 and gradually decreased towards the pre-winter season. Similar kind of variability in the LE
689 and H is also reported from the seasonally frozen ground and permafrost regions of the Tibetan
690 plateau (Gu et al., 2015; Yao et al., 2011, 2020).
691 Furthermore, in Figure 9C, during the peak summer months (June to August), the H tends to
692 decrease or became relatively stable. This is mostly due to the thawing in the seasonally frozen
693 ground resulting in a sensible heat sink (Eugster et al., 2000).
694 In the Tibetan Plateau, the main reasons for the seasonal variability of the turbulent fluxes are
695 due to the Asian monsoon and the freezing and thawing processes of the active layer (Yao et
696 al., 2011), however, in our study site, the monsoon precipitation is not a dominant factor.
697 Therefore, freeze/thaw processes are the key factor regulating the turbulent heat fluxes during
698 summers.

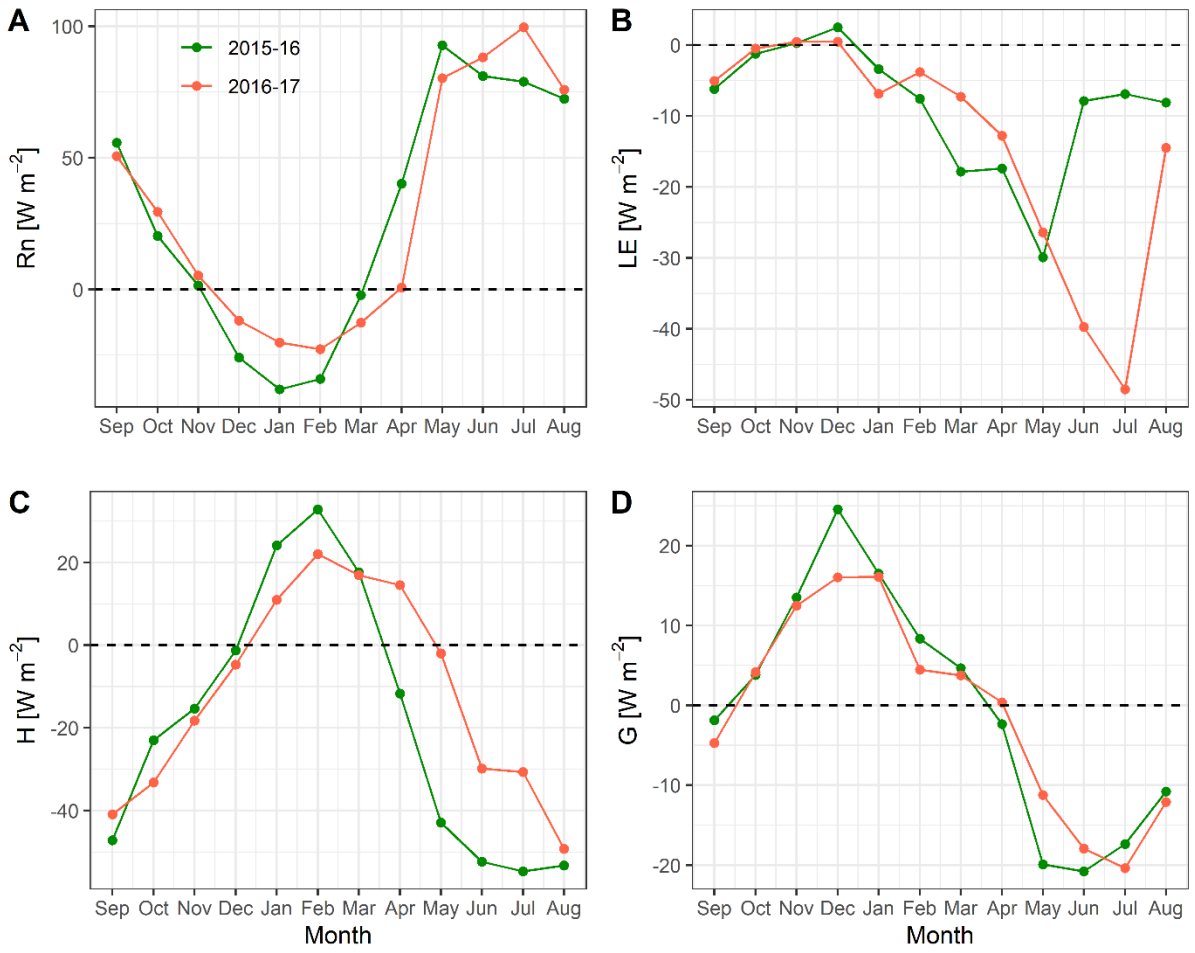

Figure 9: Comparison of estimated mean monthly surface energy balance components (W m^{-2}) (A) R_n, (B) LE, (C) H, and (D) G for the low (2015-16) and high (2016-17) snow years, at South-Pullu (4727 m a.s.l.).

5.3 Comparison with other environments

In this section, the observed radiation and estimated SEB components from our cold-arid catchment in Ladakh, India are compared with other cryospheric systems, globally (Table 5). Although aiming to represent differing permafrost environments, this comparison also includes SEB studies on glaciers for lack of additional data. In most of the studies referred here, the radiation components are measured, and the turbulent (H and LE) and ground (G) heat fluxes are modelled.

Based on the comparison, the SW_{in} at the study site is comparable with Tibetan plateau (Mölg et al., 2012; Zhang et al., 2013; Zhu et al., 2015) and significantly much higher than the values reported from other studies such as the Alps (Oerlemans and Klok, 2002; Stocker-Mittaz, 2002). The LW_{in} at the study site was comparable with values observed at Tibetan Plateau (Zhang et al., 2013; Zhu et al., 2015) and smaller than the other studies except for Antarctica. At the study site, the SW_n was the largest source of energy and LW_n the most considerable energy loss and strongly negative, and both were higher than those reported in other studies (Table 5). However, the Andes were an exception (Favier, 2004; Pellicciotti et al., 2008).

The different surface albedo (α) values help to distinguish the surface characteristics. The mean α for all the sites (Table 5) where radiation balance is measured either on bedrock or tundra vegetation was smaller than those measured over firn or ice during summer with few exceptions. Albedo ranges for glacier ice from 0.5 to 0.7 and for tundra/bedrock from 0.25 to 0.54. Comparison of RH for the study period shows that the mean measured RH (43 %) was much smaller than other regions except in the semi-arid Andes (Pellicciotti et al., 2008), where the RH was comparable. Furthermore, the mean annual precipitation in this study was also lower than in the other areas compared.

Based on the comparison of measured radiation and meteorological variables with other, better-investigated regions of the world (Table 5), it was observed that our study area is unique in terms of lower RH (43% compared to ~70% in the Alps) and cloudiness, leading to (a) Reduced LW_{in} and strongly negative LW_n (~90 W m^{-2} on average, much more than in the Alps). Hence, the high elevation cold-arid region land surfaces could be overall colder than the locations with more RH. (b) Increased SW_{in}: This will mean that sun-exposed slopes will receive more radiation and shaded ones less (less diffuse radiation) than in comparable areas, and (c) Increased cooling by stronger evaporation in wet places such as meadows. Therefore, the warm sun-exposed dry areas and colder wet places could lead to significant spatial inhomogeneity in

735 permafrost distribution. Further, it is apprehended that high incoming shortwave radiation over
736 moist high elevation surfaces may be facilitating enhanced cooling of as a result of stronger
737 evaporation.

Table 5: Comparison of mean annual observed radiation and estimated SEB components and meteorological variables with different regions of the world. (SW_{in} = Incoming shortwave radiation, SW_{out} = Outgoing shortwave radiation, albedo = α, LW_{in} = Incoming longwave radiation, LW_{out} = Outgoing longwave radiation, SW_n = Net shortwave radiation, LW_n = Net longwave radiation, RH = Relative humidity, R_n = Net radiation, LE = Latent heat flux, H = Sensible heat flux, G = Ground heat flux, SEB = energy available at surface, MAAT = Mean annual air temperature, P = Precipitation, NA = Not available). The LE, H, and G are the modelled values. All the radiation components and heat fluxes are in units of W m^{-2}.

Variable	**Leh**	**Tibetan Plateau**	**Swiss Alps**		**Tropical Andes**	**Semi-arid Andes**	**New Zealand (Alps)**	**Canada**	**Sub-Arctic**	**Greenland**	**High Arctic (Norway)**				**Antarctic**	
SW_{in}	210.4	230	136	149	239	344	140	136	101.3	110	79.5	122	78	108	124	94.2
SW_{out}	-83.4	-157	-72	-74	-116	-106	-93	-94	-25.7	-70	-39.5	-38	-42	-70	-79.7	-52.0
α (-)	0.40	0.68	0.53	0.5	0.49	0.3	0.66	0.69	0.25	0.64	0.50	0.31	0.54	0.65	0.64	0.55
LW_{in}	220.4	221	NA	260	272	252	278	248	310	246	263.7	261	254	272	NA	184.1
LW_{out}	-308.0	-277	NA	-308	-311	306	-305	-278	-349.8	-281	-299.0	-300	-286	-292	NA	-233.2
SW_n	127.0	73	64	75	123	238	48	42	75.6	40	40.0	84	36	38	44.3	42.2
LW_n	-87.6	-56	-36	-48	-39	-54	-27	-30	-39.8	-36	-35.3	-39	-32	-20	-49.2	-49.1
RH (%)	43.3	59	64	59	81	42	78	71	~75	75	74.8	83	74	77.9	50.8	69.4
R_n	39.4	17	28	27	84	184	21	12	37.1	4	4.78	45	4	18	-4.9	-6.9

LE	-11.2	-11	6	-1	-27	-19	1	-15	NA	NA	NA	NA	6.8	1	-62.1	-5.0
H	-15.6	13	36	-3	21	56	30	-5	2.9	NA	NA	-34.2	-6.9	15	28	12.1
G	-0.5	2	3	-2	NA	3	2	0.5	1.9	NA	NA	-3.5	~0.5	3	-0.12	0.2
MAAT (°C)	-2.5	-6.3	2.1	-1.1	0.3	NA	1.2	-4.2	6	-5.45	-2.86	-3.4	-5.4	-1.9	-10.2	-18.8
P (mm)	114	1250	NA	NA	970	NA	NA	NA	369	NA	581.2	800	NA	NA	NA	NA
Time period	Sep 2015 to Aug 2017	Aug 2010 to Jul 2012	Jan to Dec 2000	Feb 1997 to Jan 1998	Mar 2002 to Mar 2003	11 Dec 2005–12 Feb 2006	Oct 2010 to Sep 2012	2002-2013	Jan to Dec 2013	Aug 2003 to Aug 2007	Jan 2015 to Dec 2015	Jan to Dec 2000	Mar 2008 to Mar 2009	Sep 2001 to Sep 2006	Mar 2007 to Jan 2013	Apr 1988 to Mar 1989
Surface type	Bedrock/debris	Glacier ice	Glacier ice	Bedrock/debris	Glacier ice	Glacier ice	Glacier ice	Glacier ice	Peatland	Glacier ice	Tundra vegetation	Bedrock/debris	Tundra vegetation	Glacier ice	Ice sheet	Ice sheet
Location	Cold-arid, Ladakh	Zhadang Glacier, Tibetan Plateau	Morteratschgletsche glacier, Switzerland	Murtèl-Corvatsch rock glacier,	Antizana glacier 15, Ecuador	Juncal Norte Glacier, central Chile	Brewster Glacier, New Zealand	Haig Glacier, Canadian rocky mountains	Peatland complex Stordalen, Sweden	west Greenland ice sheet	Bayelva, Spitsbergen, Norway	Juvvasshøe, southern Norway	Svalbard, Norway	Storbreen glacier, Norway	Schirmacher Oasis, Antarctica	Dronning Maud Land, Antarctica
Elevation (m)	4727	5665	2100	2700	4890	3127	1760	2665	380	490	25	1894	25	1570	142	1150

Latitude	34.255° N	30.476° N	46.400° N	46.433° N	0.467° S	32.99056° S	44.084° S	50.717° N	68.349° N	67.100° N	78.551° N	61.676° N	78.917° N	61.600° N	70.733° S	74.481° S
Source	This Study	(Zhu et al., 2015)	(Oerlemans and Klok, 2002)	(Stocker-Mittaz, 2002)	(Favier, 2004)	(Pellicciotti et al., 2008)	(Cullen and Conway, 2015)	(Marshall, 2014)	(Stiegler et al., 2016)	(van den Broeke et al., 2008)	(Boike et al., 2018)	(Isaksen et al., 2003)	(Westermann et al., 2009)	(Giesen et al., 2009)	(Ganju and Gusain, 2017)	(Bintanja et al., 1997)

744

6 Conclusion

In the high-elevation, cold–arid regions of Ladakh significant areas of permafrost occurrence are highly likely (Wani et al., 2020) and large areas experience deep seasonal freeze-thaw. The present study is aimed at providing first insight on the surface energy balance characteristics of this permafrost environment.

For the period under study, the surface energy balance characteristics of the cold-arid site in the Indian Himalayan region show that the net radiation was the major component with a mean value of 29.7 W m^{-2}, followed by sensible heat flux (-15.6 W m^{-2}) and latent heat flux (-11.2 W m^{-2}), and the mean ground heat flux was equal to -0.5 W m^{-2}. During the study period, the partitioning of surface energy balance shows that 52% of R_n was converted into H, 38% into LE, 1% into G and 9% for melting of seasonal snow.

Among the two observation years, one was a low snow year, and the another was high, and during these low and high snow years, the energy utilised for melting seasonal snow was 4% and 14% of R_n, respectively. During both the years, the latent heat flux was highest in summer and lowest in winter, whereas the sensible heat flux was highest in post-winter and gradually decreased towards the pre-winter season. For both low and high years, the snowfall in the catchment occurred by the last week of December facilitating the ground cooling by almost three months (October to December) of sub-zero temperatures up to -20 °C. The extended snow cover during the high snow year also insulates the ground from warmer temperature until May. Therefore, the late occurrence of snow and extended snow cover could be the critical factors in controlling the thermal regime of permafrost in the area.

A comparison of observed radiation and meteorological variables with other regions of the world show that the study site/region at Ladakh have a very low relative humidity (RH) in the range of 43% compared to, e.g. ~70% in the Alps. Therefore, rarefied and dry atmosphere of the cold-arid Himalaya could be impacting the energy regime in multiple ways: (a) this results

in the reduced amount of incoming longwave radiation and strongly negative net longwave radiation, in the range of -90 W m^{-2} compared to -40 W m^{-2} in the Alps and therefore, leading to colder land surfaces as compared to the other mountain environment with higher RH, (b) higher global shortwave radiation leads to more radiation received by sun-exposed slopes than shaded ones in comparable areas and wet places such as meadows, etc. experience increased cooling as a result of stronger evaporation. However, sun-exposed dry areas could be warmer, leading to significant spatial inhomogeneity in permafrost distribution. The current study gives a first-order overview of the surface energy balance from the cold-arid Himalaya in the context of permafrost processes, and we hope this will encourage similar studies at other locations in the region, which would significantly improve the understanding of the climate from the region.

Acknowledgements

John Mohd Wani acknowledges the Ministry of Human Resource Development (MHRD) Government of India (GOI) fellowship for carrying out his PhD work. Renoj J. Thayyen thanks the National Institute of Hydrology (NIH) Roorkee and SERB (Project No. EMR/2015/000887) for funding the instrumentation in the Ganglass catchment. The first insight into the use of GEOtop permafrost spin up scheme by Joel Fiddes is highly acknowledged. We acknowledge the developers of GEOtop, for keeping the software open-source and free. The source code of the GEOtop model 2.0 (Endrizzi et al., 2014) used is freely available at https://github.com/geotopmodel/geotop/tree/se27xx. The analysis of data was performed using R (R Core Team, 2016; Wickham, 2016, 2017; Wickham and Francois, 2016; Wilke, 2019).

Conflicts of interest

The author(s) declare(s) that there is no conflict of interest.

Author contributions

JMW participated in data collection in the field, carried out the data analysis and processing, run the GEOtop model and prepared the manuscript. RJT conceived the study, arranged field instruments, organised fieldwork for instrumentation and data collection, contributed to the data analysis and manuscript preparation. CSPO assisted in data analysis and manuscript preparation. SG assisted in setting up GEOtop model, analysis of results and manuscript preparation.

801 **References**

802 Ali, S. N., Quamar, M. F., Phartiyal, B. and Sharma, A.: Need for Permafrost Researches in
803 Indian Himalaya, J. Clim. Chang., 4(1), 33–36, doi:10.3233/jcc-180004, 2018.
804 Allen, S. K., Fiddes, J., Linsbauer, A., Randhawa, S. S., Saklani, B. and Salzmann, N.:
805 Permafrost Studies in Kullu District, Himachal Pradesh, Curr. Sci., 111(3), 550–553,
806 doi:10.18520/cs/v111/i3/550-553, 2016.
807 Azam, M. F., Wagnon, P., Vincent, C., Ramanathan, A. L., Favier, V., Mandal, A. and
808 Pottakkal, J. G.: Processes governing the mass balance of Chhota Shigri Glacier (western
809 Himalaya, India) assessed by point-scale surface energy balance measurements, Cryosph.,
810 8(6), 2195–2217, doi:10.5194/tc-8-2195-2014, 2014.
811 Badescu, V., Gueymard, C. A., Cheval, S., Oprea, C., Baciu, M., Dumitrescu, A., Iacobescu,
812 F., Milos, I. and Rada, C.: Computing global and diffuse solar hourly irradiation on clear sky.
813 Review and testing of 54 models, Renew. Sustain. Energy Rev., 16(3), 1636–1656,
814 doi:10.1016/j.rser.2011.12.010, 2012.
815 Baral, P., Haq, M. A. and Yaragal, S.: Assessment of rock glaciers and permafrost distribution
816 in Uttarakhand, India, Permafr. Periglac. Process., (April 2018), 1–26, doi:10.1002/ppp.2008,
817 2019.
818 Bertoldi, G., Notarnicola, C., Leitinger, G., Endrizzi, S., Zebisch, M., Della Chiesa, S. and
819 Tappeiner, U.: Topographical and ecohydrological controls on land surface temperature in an
820 alpine catchment, Ecohydrology, 3(2), 189–204, doi:10.1002/eco.129, 2010.
821 Bhutiyani, M. R.: Mass-balance studies on Siachen Glacier in the Nubra valley, Karakoram
822 Himalaya, India, J. Glaciol., 45(149), 112–118, doi:10.3189/S0022143000003099, 1999.
823 Bhutiyani, M. R., Kale, V. S. and Pawar, N. J.: Long-term trends in maximum, minimum and
824 mean annual air temperatures across the Northwestern Himalaya during the twentieth century,
825 Clim. Change, 85(1–2), 159–177, doi:10.1007/s10584-006-9196-1, 2007.
826 Bintanja, R., Jonsson, S. and Knap, W. H.: The annual cycle of the surface energy balance of

827 Antarctic blue ice, J. Geophys. Res. Atmos., 102(D2), 1867–1881, doi:10.1029/96JD01801,
828 1997.
829 Boeckli, L., Brenning, A., Gruber, S. and Noetzli, J.: A statistical approach to modelling
830 permafrost distribution in the European Alps or similar mountain ranges, Cryosph., 6(1), 125–
831 140, doi:10.5194/tc-6-125-2012, 2012.
832 Boike, J., Wille, C. and Abnizova, A.: Climatology and summer energy and water balance of
833 polygonal tundra in the Lena River Delta, Siberia, J. Geophys. Res., 113(G3), 1–15,
834 doi:10.1029/2007JG000540, 2008.
835 Boike, J., Juszak, I., Lange, S., Chadburn, S., Burke, E., Overduin, P. P., Roth, K., Ippisch, O.,
836 Bornemann, N., Stern, L., Gouttevin, I., Hauber, E. and Westermann, S.: A 20-year record
837 (1998-2017) of permafrost, active layer and meteorological conditions at a high Arctic
838 permafrost research site (Bayelva, Spitsbergen), Earth Syst. Sci. Data, 10(1), 355–390,
839 doi:10.5194/essd-10-355-2018, 2018.
840 Bolch, T., Kulkarni, A., Kääb, A., Huggel, C., Paul, F., Cogley, J. G., Frey, H., Kargel, J. S.,
841 Fujita, K., Scheel, M. and others: The state and fate of Himalayan glaciers, Science (80-.).,
842 336(6079), 310–314, doi:10.1126/science.1215828, 2012.
843 Bolch, T., Shea, J. M., Liu, S., Azam, F. M., Gao, Y., Gruber, S., Immerzeel, W. W., Kulkarni,
844 A., Li, H., Tahir, A. A., Zhang, G. and Zhang, Y.: Status and Change of the Cryosphere in the
845 Extended Hindu Kush Himalaya Region, in The Hindu Kush Himalaya Assessment, edited by
846 P. Wester, A. Mishra, A. Mukherji, and A. B. Shrestha, pp. 209–255, Springer, Cham., 2019.
847 Bommer, C., Phillips, M. and Arenson, L. U.: Practical recommendations for planning,
848 constructing and maintaining infrastructure in mountain permafrost, Permafr. Periglac.
849 Process., 21(1), 97–104, doi:10.1002/ppp.679, 2010.
850 van den Broeke, M., van As, D., Reijmer, C. and van de Wal, R.: Assessing and Improving the
851 Quality of Unattended Radiation Observations in Antarctica, J. Atmos. Ocean. Technol., 21(9),

852 1417–1431, doi:10.1175/1520-0426(2004)021<1417:AAITQO>2.0.CO;2, 2004.
853 van den Broeke, M., Smeets, P., Ettema, J. and Munneke, P. K.: Surface radiation balance in
854 the ablation zone of the west Greenland ice sheet, J. Geophys. Res., 113(D13), 1–14,
855 doi:10.1029/2007JD009283, 2008.
856 Brutsaert, W.: A theory for local evaporation (or heat transfer) from rough and smooth surfaces
857 at ground level, Water Resour. Res., 11(4), 543–550, doi:10.1029/WR011i004p00543, 1975.
858 Cao, B., Quan, X., Brown, N., Stewart-Jones, E. and Gruber, S.: GlobSim (v1.0): Deriving
859 meteorological time series for point locations from multiple global reanalyses, Geosci. Model
860 Dev. Discuss., (July), 1–29, doi:10.5194/gmd-2019-157, 2019.
861 Carslaw, D. C. and Ropkins, K.: openair — An R package for air quality data analysis, Environ.
862 Model. Softw., 27–28, 52–61, doi:10.1016/j.envsoft.2011.09.008, 2012.
863 Chen, B., Luo, S., Lü, S., Yu, Z. and Ma, D.: Effects of the soil freeze-thaw process on the
864 regional climate of the Qinghai-Tibet Plateau, Clim. Res., 59(3), 243–257,
865 doi:10.3354/cr01217, 2014.
866 Chiesa, D. D., Bertoldi, G., Niedrist, G., Obojes, N., Endrizzi, S., Albertson, J. D., Wohlfahrt,
867 G., Hörtnagl, L. and Tappeiner, U.: Modelling changes in grassland hydrological cycling along
868 an elevational gradient in the Alps, Ecohydrology, 7(6), 1453–1473, doi:10.1002/eco.1471,
869 2014.
870 Cosenza, P., Guérin, R. and Tabbagh, A.: Relationship between thermal conductivity and water
871 content of soils using numerical modelling, Eur. J. Soil Sci., 54(3), 581–588,
872 doi:10.1046/j.1365-2389.2003.00539.x, 2003.
873 Cullen, N. J. and Conway, J. P.: A 22 month record of surface meteorology and energy balance
874 from the ablation zone of Brewster Glacier, New Zealand, J. Glaciol., 61(229), 931–946,
875 doi:10.3189/2015JoG15J004, 2015.
876 Dall'Amico, M., Endrizzi, S., Gruber, S. and Rigon, R.: A robust and energy-conserving model

877 of freezing variably-saturated soil, Cryosph., 5(2), 469–484, doi:10.5194/tc-5-469-2011,
878 2011a.
879 Dall'Amico, M., Endrizzi, S. and Rigon, R.: Snow mapping of an alpine catchment through
880 the hydrological model GEOtop, in Proceedings Conference Eaux en montagne, Lyon, pp. 16–
881 17., 2011b.
882 Dall'Amico, M., Endrizzi, S. and Tasin, S.: MYSNOWMAPS: OPERATIVE HIGH-
883 RESOLUTION REAL-TIME SNOW MAPPING, in Proceedings, International Snow Science
884 Workshop, pp. 328–332, Innsbruck, Austria., 2018.
885 Endrizzi, S.: Snow cover modelling at a local and distributed scale over complex terrain,
886 University of Trento., 2007.
887 Endrizzi, S., Gruber, S., Dall'Amico, M. and Rigon, R.: GEOtop 2.0: simulating the combined
888 energy and water balance at and below the land surface accounting for soil freezing, snow
889 cover and terrain effects, Geosci. Model Dev., 7(6), 2831–2857, doi:10.5194/gmd-7-2831-
890 2014, 2014.
891 Engel, M., Notarnicola, C., Endrizzi, S. and Bertoldi, G.: Snow model sensitivity analysis to
892 understand spatial and temporal snow dynamics in a high-elevation catchment, Hydrol.
893 Process., 31(23), 4151–4168, doi:10.1002/hyp.11314, 2017.
894 Eugster, W., Rouse, W. R., Pielke Sr, R. A., Mcfadden, J. P., Baldocchi, D. D., Kittel, T. G. F.,
895 Chapin, F. S., Liston, G. E., Vidale, P. L., Vaganov, E. and Chambers, S.: Land-atmosphere
896 energy exchange in Arctic tundra and boreal forest: available data and feedbacks to climate,
897 Glob. Chang. Biol., 6(S1), 84–115, doi:10.1046/j.1365-2486.2000.06015.x, 2000.
898 Favier, V.: One-year measurements of surface heat budget on the ablation zone of Antizana
899 Glacier 15, Ecuadorian Andes, J. Geophys. Res., 109(D18), 1–15, doi:10.1029/2003JD004359,
900 2004.
901 Fiddes, J. and Gruber, S.: TopoSUB: a tool for efficient large area numerical modelling in

902 complex topography at sub-grid scales, Geosci. Model Dev., 5(5), 1245–1257,
903 doi:10.5194/gmd-5-1245-2012, 2012.
904 Fiddes, J., Endrizzi, S. and Gruber, S.: Large-area land surface simulations in heterogeneous
905 terrain driven by global data sets: application to mountain permafrost, Cryosph., 9(1), 411–
906 426, doi:10.5194/tc-9-411-2015, 2015.
907 Ganju, A. and Gusain, H. S.: Six Years Observations ond Analysis of Radiation Parameters
908 and Surface Energy Fluxes on Ice Sheet Near 'Maitri'Research Station, East Antarctica, Proc.
909 Indian Natl. Sci. Acad., 83(2), 449–460, 2017.
910 Gao, T., Zhang, T., Guo, H., Hu, Y., Shang, J. and Zhang, Y.: Impacts of the active layer on
911 runoff in an upland permafrost basin, northern Tibetan Plateau, edited by J. A. Añel, PLoS
912 One, 13(2), 1–15, doi:10.1371/journal.pone.0192591, 2018.
913 Garratt, J. R.: The atmospheric boundary layer. Cambridge atmospheric and space science
914 series, Cambridge University Press., 1994.
915 Giesen, R. H., Andreassen, L. M., van den Broeke, M. R. and Oerlemans, J.: Comparison of
916 the meteorology and surface energy balance at Storbreen and Midtdalsbreen, two glaciers in
917 southern Norway, Cryosph., 3(1), 57–74, doi:10.5194/tc-3-57-2009, 2009.
918 Gruber, S. and Haeberli, W.: Permafrost in steep bedrock slopes and its temperature-related
919 destabilization following climate change, J. Geophys. Res., 112(F2), 1–10,
920 doi:10.1029/2006JF000547, 2007.
921 Gruber, S., Hoelzle, M. and Haeberli, W.: Permafrost thaw and destabilization of Alpine rock
922 walls in the hot summer of 2003, Geophys. Res. Lett., 31(L13504), 1–4,
923 doi:10.1029/2004GL020051, 2004.
924 Gruber, S., Fleiner, R., Guegan, E., Panday, P., Schmid, M. O., Stumm, D., Wester, P., Zhang,
925 Y. and Zhao, L.: Review article: Inferring permafrost and permafrost thaw in the mountains of
926 the Hindu Kush Himalaya region, Cryosph., 11(1), 81–99, doi:10.5194/tc-11-81-2017, 2017.

927 Gu, L., Yao, J., Hu, Z. and Zhao, L.: Comparison of the surface energy budget between regions
928 of seasonally frozen ground and permafrost on the Tibetan Plateau, Atmos. Res., 153, 553–
929 564, doi:10.1016/j.atmosres.2014.10.012, 2015.
930 Gubler, S.: Measurement Variability and Model Uncertainty in Mountain Permafrost Research,
931 University of Zurich., 2013.
932 Gubler, S., Gruber, S. and Purves, R. S.: Uncertainties of parameterized surface downward
933 clear-sky shortwave and all-sky longwave radiation., Atmos. Chem. Phys., 12(11), 5077–5098,
934 doi:10.5194/acp-12-5077-2012, 2012.
935 Gubler, S., Endrizzi, S., Gruber, S. and Purves, R. S.: Sensitivities and uncertainties of modeled
936 ground temperatures in mountain environments, Geosci. Model Dev., 6(4), 1319–1336,
937 doi:10.5194/gmd-6-1319-2013, 2013.
938 Gueymard, C. A.: Clear-sky irradiance predictions for solar resource mapping and large-scale
939 applications: Improved validation methodology and detailed performance analysis of 18
940 broadband radiative models, Sol. Energy, 86(8), 2145–2169,
941 doi:10.1016/j.solener.2011.11.011, 2012.
942 Gupta, H. V., Bastidas, L. A., Sorooshian, S., Shuttleworth, W. J. and Yang, Z. L.: Parameter
943 estimation of a land surface scheme using multicriteria methods, J. Geophys. Res. Atmos.,
944 104(D16), 19491–19503, doi:10.1029/1999JD900154, 1999.
945 Haeberli, W., Noetzli, J., Arenson, L., Delaloye, R., Gärtner-Roer, I., Gruber, S., Isaksen, K.,
946 Kneisel, C., Krautblatter, M. and Phillips, M.: Mountain permafrost: development and
947 challenges of a young research field, J. Glaciol., 56(200), 1043–1058,
948 doi:10.3189/002214311796406121, 2010.
949 Harris, C., Davies, M. C. R. and Etzelmüller, B.: The assessment of potential geotechnical
950 hazards associated with mountain permafrost in a warming global climate, Permafr. Periglac.
951 Process., 12(1), 145–156, doi:10.1002/ppp.376, 2001.

Hasler, A., Geertsema, M., Foord, V., Gruber, S. and Noetzli, J.: The influence of surface characteristics, topography and continentality on mountain permafrost in British Columbia, Cryosph., 9(3), 1025–1038, doi:10.5194/tc-9-1025-2015, 2015.

Hingerl, L., Kunstmann, H., Wagner, S., Mauder, M., Bliefernicht, J. and Rigon, R.: Spatio-temporal variability of water and energy fluxes - a case study for a mesoscale catchment in pre-alpine environment, Hydrol. Process., 30(21), 3804–3823, doi:10.1002/hyp.10893, 2016.

Hock, R., Rasul, G., Adler, C., Cáceres, B., Gruber, S., Hirabayashi, Y., Jackson, M., Kääb, A., Kang, S., Kutuzov, S., Milner, A., Molau, U., Morin, S., Orlove, B. and Steltzer, H.: High Mountain Areas. In: IPCC Special Report on the Ocean and Cryosphere in a Changing Climate [H.-O. Pörtner, D.C. Roberts, V. Masson-Delmotte, P. Zhai, M. Tignor, E. Poloczanska, K. Mintenbeck, A. Alegría, M. Nicolai, A. Okem, J. Petzold, B. Rama, N.M., 2019.

Hu, G., Zhao, L., Li, R., Wu, X., Wu, T., Zhu, X., Pang, Q., Liu, G. yue, Du, E., Zou, D., Hao, J. and Li, W.: Simulation of land surface heat fluxes in permafrost regions on the Qinghai-Tibetan Plateau using CMIP5 models, Atmos. Res., 220, 155–168, doi:10.1016/j.atmosres.2019.01.006, 2019.

Immerzeel, W. W., van Beek, L. P. H. and Bierkens, M. F. P.: Climate Change Will Affect the Asian Water Towers, Science (80-.)., 328(5984), 1382–1385, doi:10.1126/science.1183188, 2010.

Immerzeel, W. W., van Beek, L. P. H., Konz, M., Shrestha, A. B. and Bierkens, M. F. P.: Hydrological response to climate change in a glacierized catchment in the Himalayas, Clim. Change, 110(3–4), 721–736, doi:10.1007/s10584-011-0143-4, 2012.

Immerzeel, W. W., Wanders, N., Lutz, A. F., Shea, J. M. and Bierkens, M. F. P.: Reconciling high-altitude precipitation in the upper Indus basin with glacier mass balances and runoff, Hydrol. Earth Syst. Sci., 19(11), 4673–4687, doi:10.5194/hess-19-4673-2015, 2015.

Isaksen, K., Heggem, E. S. F., Bakkehøi, S., Ødegård, R. S., Eiken, T., Etzelmüller, B. and

977 Sollid, J. L.: Mountain permafrost and energy balance on Juvvasshøe, southern Norway, in
978 Eight International Conference on Permafrost, vol. 1, edited by M. Phillips, S. Springman, and
979 L. Arenson, pp. 467–472, Swets & Zeitlinger, Lisse, Zurich, Switzerland., 2003.
980 Jordan, R. E., Andreas, E. L. and Makshtas, A. P.: Heat budget of snow-covered sea ice at
981 North Pole 4, J. Geophys. Res. Ocean., 104(C4), 7785–7806, doi:10.1029/1999JC900011,
982 1999.
983 Kaser, G., Grosshauser, M. and Marzeion, B.: Contribution potential of glaciers to water
984 availability in different climate regimes, Proc. Natl. Acad. Sci., 107(47), 20223–20227,
985 doi:10.1073/pnas.1008162107, 2010.
986 Kodama, Y., Sato, N., Yabuki, H., Ishii, Y., Nomura, M. and Ohata, T.: Wind direction
987 dependency of water and energy fluxes and synoptic conditions over a tundra near Tiksi,
988 Siberia, Hydrol. Process., 21(15), 2028–2037, doi:10.1002/hyp.6712, 2007.
989 Langer, M., Westermann, S., Muster, S., Piel, K. and Boike, J.: The surface energy balance of
990 a polygonal tundra site in northern Siberia - Part 2: Winter, Cryosphere, 5(2), 509–524,
991 doi:10.5194/tc-5-509-2011, 2011a.
992 Langer, M., Westermann, S., Muster, S., Piel, K. and Boike, J.: The surface energy balance of
993 a polygonal tundra site in northern Siberia – Part 1: Spring to fall, Cryosph., 5(1), 151–171,
994 doi:10.5194/tc-5-151-2011, 2011b.
995 Lloyd, C. R., Harding, R. J., Friborg, T. and Aurela, M.: Surface fluxes of heat and water
996 vapour from sites in the European Arctic, Theor. Appl. Climatol., 70(1–4), 19–33,
997 doi:10.1007/s007040170003, 2001.
998 Lone, S. A., Jeelani, G., Deshpande, R. D. and Mukherjee, A.: Stable isotope (δ18O and δD)
999 dynamics of precipitation in a high altitude Himalayan cold desert and its surroundings in Indus
1000 river basin, Ladakh, Atmos. Res., 221(October 2018), 46–57,
1001 doi:10.1016/j.atmosres.2019.01.025, 2019.

1002 Lunardini, V. J.: Heat transfer in cold climates, Van Nostrand Reinhold Company., 1981.
1003 Lutz, A. F., Immerzeel, W. W., Shrestha, A. B. and Bierkens, M. F. P.: Consistent increase in
1004 High Asia's runoff due to increasing glacier melt and precipitation, Nat. Clim. Chang., 4(7),
1005 587–592, doi:10.1038/nclimate2237, 2014.
1006 Lynch, A. H., Chapin, F. S., Hinzman, L. D., Wu, W., Lilly, E., Vourlitis, G. and Kim, E.:
1007 Surface Energy Balance on the Arctic Tundra: Measurements and Models, J. Clim., 12(8),
1008 2585–2606, doi:10.1175/1520-0442(1999)012<2585:SEBOTA>2.0.CO;2, 1999.
1009 MacDonell, S., Kinnard, C., Mölg, T., Nicholson, L. and Abermann, J.: Meteorological drivers
1010 of ablation processes on a cold glacier in the semi-arid Andes of Chile, Cryosph., 7(5), 1513–
1011 1526, doi:10.5194/tc-7-1513-2013, 2013.
1012 Mair, E., Leitinger, G., Della Chiesa, S., Niedrist, G., Tappeiner, U. and Bertoldi, G.: A simple
1013 method to combine snow height and meteorological observations to estimate winter
1014 precipitation at sub-daily resolution, Hydrol. Sci. J., 61(11), 2050–2060,
1015 doi:10.1080/02626667.2015.1081203, 2016.
1016 Marshall, S. J.: Meltwater run-off from Haig Glacier, Canadian Rocky Mountains,
1017 2002–2013, Hydrol. Earth Syst. Sci., 18(12), 5181–5200, doi:10.5194/hess-
1018 18-5181-2014, 2014.
1019 Martin, E. and Lejeune, Y.: Turbulent fluxes above the snow surface, Ann. Glaciol., 26(1),
1020 179–183, doi:10.3189/1998AoG26-1-179-183, 1998.
1021 Mauder, M., Genzel, S., Fu, J., Kiese, R., Soltani, M., Steinbrecher, R., Zeeman, M., Banerjee,
1022 T., De Roo, F. and Kunstmann, H.: Evaluation of energy balance closure adjustment methods
1023 by independent evapotranspiration estimates from lysimeters and hydrological simulations,
1024 Hydrol. Process., 32(1), 39–50, doi:10.1002/hyp.11397, 2018.
1025 McBean, G. A. and Miyake, M.: Turbulent transfer mechanisms in the atmospheric surface
1026 layer, Q. J. R. Meteorol. Soc., 98(416), 383–398, doi:10.1002/qj.49709841610, 1972.

1027 Mittaz, C., Hoelzle, M. and Haeberli, W.: First results and interpretation of energy-flux
1028 measurements over Alpine permafrost, Ann. Glaciol., 31, 275–280,
1029 doi:10.3189/172756400781820363, 2000.
1030 Mölg, T.: Ablation and associated energy balance of a horizontal glacier surface on
1031 Kilimanjaro, J. Geophys. Res., 109(D16), D16104, doi:10.1029/2003JD004338, 2004.
1032 Mölg, T., Maussion, F., Yang, W. and Scherer, D.: The footprint of Asian monsoon dynamics
1033 in the mass and energy balance of a Tibetan glacier, Cryosph., 6(6), 1445–1461,
1034 doi:10.5194/tc-6-1445-2012, 2012.
1035 Monin, A. S. and Obukhov, A. M.: Basic laws of turbulent mixing in the atmosphere near the
1036 ground, Tr. Akad. Nauk SSSR Geofiz. Inst, 24(151), 163–187, 1954.
1037 Mu, C., Li, L., Wu, X., Zhang, F., Jia, L., Zhao, Q. and Zhang, T.: Greenhouse gas released
1038 from the deep permafrost in the northern Qinghai-Tibetan Plateau, Sci. Rep., 8(1), 1–9,
1039 doi:10.1038/s41598-018-22530-3, 2018.
1040 Nash, J. E. and Sutcliffe, J. V.: River flow forecasting through conceptual models part I — A
1041 discussion of principles, J. Hydrol., 10(3), 282–290, doi:10.1016/0022-1694(70)90255-6,
1042 1970.
1043 Nicholson, L. I., Prinz, R., Mölg, T. and Kaser, G.: Micrometeorological conditions and surface
1044 mass and energy fluxes on Lewis Glacier, Mt Kenya, in relation to other tropical glaciers,
1045 Cryosph., 7(4), 1205–1225, doi:10.5194/tc-7-1205-2013, 2013.
1046 Oerlemans, J. and Klok, E. J.: Energy Balance of a Glacier Surface: Analysis of Automatic
1047 Weather Station Data from the Morteratschgletscher, Switzerland, Arctic, Antarct. Alp. Res.,
1048 34(4), 477–485, doi:10.1080/15230430.2002.12003519, 2002.
1049 Ohmura, A.: Climate and energy balance on the arctic tundra, J. Climatol., 2(1), 65–84,
1050 doi:10.1002/joc.3370020106, 1982.
1051 Ohmura, A.: Comparative energy balance study for arctic tundra, sea surface glaciers and

boreal forests, GeoJournal, 8(3), 221–228, doi:10.1007/BF00446471, 1984.

Oke, T. R.: Boundary Layer Climates, Routledge., 2002.

Pandey, P.: Inventory of rock glaciers in Himachal Himalaya, India using high-resolution Google Earth imagery, Geomorphology, 340, 103–115, doi:10.1016/j.geomorph.2019.05.001, 2019.

Pellicciotti, F., Helbing, J., Rivera, A., Favier, V., Corripio, J., Araos, J., Sicart, J.-E. and Carenzo, M.: A study of the energy balance and melt regime on Juncal Norte Glacier, semi-arid Andes of central Chile, using melt models of different complexity, Hydrol. Process., 22(19), 3980–3997, doi:10.1002/hyp.7085, 2008.

PERMOS: Permafrost in Switzerland 2014/2015 to 2017/2018. Noetzli, J., Pellet, C. and Staub, B. (eds.), Glaciological Report Permafrost No. 16-19 of the Cryospheric Commission of the Swiss Academy of Sciences, 104 pp., 2019.

Pogliotti, P.: Influence of snow cover on MAGST over complex morphologies in mountain permafrost regions, University of Torino, Torino., 2011.

Pritchard, H. D.: Asia's shrinking glaciers protect large populations from drought stress, Nature, 569(7758), 649–654, doi:10.1038/s41586-019-1240-1, 2019.

R Core Team: R: A Language and Environment for Statistical Computing, [online] Available from: https://www.r-project.org/, 2016.

Rasmussen, R., Baker, B., Kochendorfer, J., Meyers, T., Landolt, S., Fischer, A. P., Black, J., Thériault, J. M., Kucera, P., Gochis, D., Smith, C., Nitu, R., Hall, M., Ikeda, K. and Gutmann, E.: How Well Are We Measuring Snow: The NOAA/FAA/NCAR Winter Precipitation Test Bed, Bull. Am. Meteorol. Soc., 93(6), 811–829, doi:10.1175/BAMS-D-11-00052.1, 2012.

Rastogi, S. P. and Narayan, S.: Permafrost areas in Tso Kar Basin, in Symposium for Snow, Ice and Glaciers, March 1999, pp. 315–319, Geological Survey of India Special Publication 53., 1999.

Rigon, R., Bertoldi, G. and Over, T. M.: GEOtop: A Distributed Hydrological Model with Coupled Water and Energy Budgets, J. Hydrometeorol., 7(3), 371–388, doi:10.1175/JHM497.1, 2006.

Roberts, K. E., Lamoureux, S. F., Kyser, T. K., Muir, D. C. G., Lafrenière, M. J., Iqaluk, D., Pieńkowski, A. J. and Normandeau, A.: Climate and permafrost effects on the chemistry and ecosystems of High Arctic Lakes, Sci. Rep., 7(1), 1–8, doi:10.1038/s41598-017-13658-9, 2017.

Roesch, A., Wild, M., Pinker, R. and Ohmura, A.: Comparison of spectral surface albedos and their impact on the general circulation model simulated surface climate, J. Geophys. Res., 107(D14), 4221, doi:10.1029/2001JD000809, 2002.

Salzmann, N., Nötzli, J., Hauck, C., Gruber, S., Hoelzle, M. and Haeberli, W.: Ground surface temperature scenarios in complex high-mountain topography based on regional climate model results, J. Geophys. Res., 112(F2), 1–10, doi:10.1029/2006JF000527, 2007.

Schmid, M.-O., Baral, P., Gruber, S., Shahi, S., Shrestha, T., Stumm, D. and Wester, P.: Assessment of permafrost distribution maps in the Hindu Kush Himalayan region using rock glaciers mapped in Google Earth, Cryosph., 9(6), 2089–2099, doi:10.5194/tc-9-2089-2015, 2015.

Sellers, W. D.: Physical climatology, The University of Chicago Press., 1965.

Singh, N., Singhal, M., Chhikara, S., Karakoti, I., Chauhan, P. and Dobhal, D. P.: Radiation and energy balance dynamics over a rapidly receding glacier in the central Himalaya, Int. J. Climatol., 40(1), 400–420, doi:10.1002/joc.6218, 2020.

Soltani, M., Laux, P., Mauder, M. and Kunstmann, H.: Inverse distributed modelling of streamflow and turbulent fluxes: A sensitivity and uncertainty analysis coupled with automatic optimization, J. Hydrol., 571, 856–872, doi:10.1016/j.jhydrol.2019.02.033, 2019.

Stiegler, C., Johansson, M., Christensen, T. R., Mastepanov, M. and Lindroth, A.: Tundra

permafrost thaw causes significant shifts in energy partitioning, Tellus B Chem. Phys. Meteorol., 68(1), 1–11, doi:10.3402/tellusb.v68.30467, 2016.

Stocker-Mittaz, C.: Permafrost Distribution Modeling Based on Energy Balance Data, University of Zurich, Switzerland., 2002.

Strugnell, N. C. and Lucht, W.: An Algorithm to Infer Continental-Scale Albedo from AVHRR Data, Land Cover Class, and Field Observations of Typical BRDFs, J. Clim., 14(7), 1360–1376, doi:10.1175/1520-0442(2001)014<1360:AATICS>2.0.CO;2, 2001.

Stull, R. B.: An Introduction to Boundary Layer Meteorology, Springer Netherlands, Dordrecht., 1988.

Thakur, V. C.: Regional framework and geodynamic evolution of the Indus-Tsangpo suture zone in the Ladakh Himalayas, Trans. R. Soc. Edinb. Earth Sci., 72(2), 89–97, doi:10.1017/S0263593300009925, 1981.

Thayyen, R. J.: Ground ice melt in the catchment runoff in the Himalayan cold-arid system, in IGS Symposium on Glaciology in High-Mountain Asia, Kathmandu, Nepal, 1-6 March 2015, Kathmandu, Nepal., 2015.

Thayyen, R. J.: Hydrology of the Cold-Arid Himalaya, in Himalayan Weather and Climate and their Impact on the Environment, pp. 399–417, Springer International Publishing, Cham., 2020.

Thayyen, R. J. and Dimri, A. P.: Factors controlling Slope Environmental Lapse Rate (SELR) of temperature in the monsoon and cold-arid glacio-hydrological regimes of the Himalaya, Cryosph. Discuss., 8(6), 5645–5686, doi:10.5194/tcd-8-5645-2014, 2014.

Thayyen, R. J. and Gergan, J. T.: Role of glaciers in watershed hydrology: a preliminary study of a “Himalayan catchment,” Cryosph., 4(1), 115–128, doi:10.5194/tc-4-115-2010, 2010.

Thayyen, R. J., Dimri, A. P., Kumar, P. and Agnihotri, G.: Study of cloudburst and flash floods around Leh, India, during August 4–6, 2010, Nat. Hazards, 65(3), 2175–2204, doi:10.1007/s11069-012-0464-2, 2013.

Thayyen, R. J., Rai, S. P. and Goel, M. K.: Glaciological studies of Phuche glacier, Ladakh Range., 2015.

Wang, G., Li, Y., Wu, Q. and Wang, Y.: Impacts of permafrost changes on alpine ecosystem in Qinghai-Tibet Plateau, Sci. China Ser. D Earth Sci., 49(11), 1156–1169, doi:10.1007/s11430-006-1156-0, 2006.

Wang, X., Chen, R. and Yang, Y.: Effects of Permafrost Degradation on the Hydrological Regime in the Source Regions of the Yangtze and Yellow Rivers, China, Water, 9(11), 1–13, doi:10.3390/w9110897, 2017.

Wani, J. M., Thayyen, R. J., Gruber, S., Ojha, C. S. P. and Stumm, D.: Single-year thermal regime and inferred permafrost occurrence in the upper Ganglass catchment of the cold-arid Himalaya, Ladakh, India, Sci. Total Environ., 703, doi:10.1016/j.scitotenv.2019.134631, 2020.

Westermann, S., Lüers, J., Langer, M., Piel, K. and Boike, J.: The annual surface energy budget of a high-arctic permafrost site on Svalbard, Norway, Cryosph., 3(2), 245–263, doi:10.5194/tc-3-245-2009, 2009.

Wickham, H.: ggplot2: Elegant Graphics for Data Analysis, [online] Available from: https://ggplot2.tidyverse.org, 2016.

Wickham, H.: tidyverse: Easily Install and Load the “Tidyverse”., [online] Available from: https://cran.r-project.org/package=tidyverse, 2017.

Wickham, H. and Francois, R.: dplyr: A Grammar of Data Manipulation, [online] Available from: https://cran.r-project.org/package=dplyr, 2016.

Wilke, C. O.: cowplot: Streamlined Plot Theme and Plot Annotations for “ggplot2,” [online] Available from: https://cran.r-project.org/package=cowplot, 2019.

Woo, M.-K., Kane, D. L., Carey, S. K. and Yang, D.: Progress in permafrost hydrology in the new millennium, Permafr. Periglac. Process., 19(2), 237–254, doi:10.1002/ppp.613, 2008.

Wünnemann, B., Reinhardt, C., Kotlia, B. S. and Riedel, F.: Observations on the relationship

between lake formation, permafrost activity and lithalsa development during the last 20 000 years in the Tso Kar basin, Ladakh, India, Permafr. Periglac. Process., 19(4), 341–358, doi:10.1002/ppp.631, 2008.

Xia, Z.: Simulation of the Bare Soil Surface Energy Balance at the Tongyu Reference Site in Semiarid Area of North China, Atmos. Ocean. Sci. Lett., 3(6), 330–335, doi:10.1080/16742834.2010.11446892, 2010.

Yang, D., Goodison, B. E., Metcalfe, J. R., Louie, P., Leavesley, G., Emerson, D., Hanson, C. L., Golubev, V. S., Elomaa, E., Gunther, T., Pangburn, T., Kang, E. and Milkovic, J.: Quantification of precipitation measurement discontinuity induced by wind shields on national gauges, Water Resour. Res., 35(2), 491–508, doi:10.1029/1998WR900042, 1999.

Yao, J., Zhao, L., Ding, Y., Gu, L., Jiao, K., Qiao, Y. and Wang, Y.: The surface energy budget and evapotranspiration in the Tanggula region on the Tibetan Plateau, Cold Reg. Sci. Technol., 52(3), 326–340, doi:10.1016/j.coldregions.2007.04.001, 2008.

Yao, J., Zhao, L., Gu, L., Qiao, Y. and Jiao, K.: The surface energy budget in the permafrost region of the Tibetan Plateau, Atmos. Res., 102(4), 394–407, doi:10.1016/j.atmosres.2011.09.001, 2011.

Yao, J., Gu, L., Yang, C., Chen, H., Wang, J., Ding, Y., Li, R., Zhao, L., Xiao, Y., Qiao, Y., Shi, J. and Chen, C.: Estimation of surface energy fluxes in the permafrost region of the Tibetan Plateau based on situ measurements and the <scp>SEBS</scp> model, Int. J. Climatol., joc.6551, doi:10.1002/joc.6551, 2020.

Ye, Z. and Pielke, R. A.: Atmospheric Parameterization of Evaporation from Non-Plant-covered Surfaces, J. Appl. Meteorol., 32(7), 1248–1258, doi:10.1175/1520-0450(1993)032<1248:APOEFN>2.0.CO;2, 1993.

Zanotti, F., Endrizzi, S., Bertoldi, G. and Rigon, R.: The GEOTOP snow module, Hydrol. Process., 18(18), 3667–3679, doi:10.1002/hyp.5794, 2004.

Zhang, G., Kang, S., Fujita, K., Huintjes, E., Xu, J., Yamazaki, T., Haginoya, S., Wei, Y., Scherer, D., Schneider, C. and Yao, T.: Energy and mass balance of Zhadang glacier surface, central Tibetan Plateau, J. Glaciol., 59(213), 137–148, doi:10.3189/2013JoG12J152, 2013.

Zhao, L., Cheng, G., Li, S., Zhao, X. and Wang, S.: Thawing and freezing processes of active layer in Wudaoliang region of Tibetan Plateau, Chinese Sci. Bull., 45(23), 2181–2187, doi:10.1007/BF02886326, 2000.

Zhu, M., Yao, T., Yang, W., Maussion, F., Huintjes, E. and Li, S.: Energy- and mass-balance comparison between Zhadang and Parlung No. 4 glaciers on the Tibetan Plateau, J. Glaciol., 61(227), 595–607, doi:10.3189/2015JoG14J206, 2015.